



Provided by the author(s) and University of Galway in accordance with publisher policies. Please cite the published version when available.

Title	A review of thermal, microstructural and constitutive modelling of 9Cr steel for power plant applications: Towards a through-process model for structural integrity of welded connections
Author(s)	Mac Ardghail, Padraig; Leen, Sean B.; Harrison, Noel M.
Publication Date	2020-01-01
Publication Information	Ardghail, P. Mac, Leen, S. B., & Harrison, N. (2020). A review of thermal, microstructural and constitutive modelling of 9Cr steel for power plant applications: Towards a through-process model for structural integrity of welded connections. <i>International Journal of Pressure Vessels and Piping</i> , 104037. doi: <a href="https://doi.org/10.1016/j.ijpvp.2019.104037">https://doi.org/10.1016/j.ijpvp.2019.104037</a>
Publisher	Elsevier
Link to publisher's version	<a href="https://doi.org/10.1016/j.ijpvp.2019.104037">https://doi.org/10.1016/j.ijpvp.2019.104037</a>
Item record	<a href="http://hdl.handle.net/10379/15696">http://hdl.handle.net/10379/15696</a>
DOI	<a href="http://dx.doi.org/10.1016/j.ijpvp.2019.104037">http://dx.doi.org/10.1016/j.ijpvp.2019.104037</a>

Downloaded 2024-04-23T14:47:26Z

Some rights reserved. For more information, please see the item record link above.



# **A review of thermal, microstructural and constitutive modelling of 9Cr steel for power plant applications: Towards a through-process model for structural integrity of welded connections**

P. Mac Ardghail<sup>1,3</sup>, S.B. Leen<sup>1,2,3</sup>, N. Harrison<sup>1,2,3</sup>

<sup>1</sup> Mechanical Engineering, School of Engineering, National University of Ireland Galway, Galway, Ireland.

<sup>2</sup> I-Form Advanced Manufacturing Research Centre, Ireland

<sup>3</sup> Ryan Institute for Environmental, Marine and Energy Research, National University of Ireland Galway, Galway, Ireland

## **Abstract**

Life prediction for 9Cr steel welded components is an important issue facing power plant as it moves from steady-state, base-load operation to transient, flexible operation. Welding and heat-treatment of 9Cr components alters the steel microstructure to produce a heat-affected zone, which is susceptible to early failure under creep and high-temperature cyclic conditions. Optimal welding and heat treatment processes cannot feasibly be identified experimentally but finite element simulation is a practical solution to this problem. A review of modelling methodologies for welding, heat treatment and in-service operation in thermal power plant for 9Cr steel is presented here. The authors consider that macro-scale, physically-based models are the most promising models currently available since they account for changes in material microstructure while still being practical for simulations involving component-sized FE geometries.

## **1. Introduction**

This work encompasses welding simulation, microstructure evolution modelling and constitutive modelling of welded 9Cr power plant components. To date, most models published in this field have focused on one or two of these modelling aspects, e.g. combining thermal and constitutive modelling [1, 2], microstructural and constitutive modelling [3], thermal and microstructural modelling [4]. The three modelling aspects used together in a single analysis will be referred to in this work as ‘through-process’ modelling. The concept of through-process modelling is to capture the complete evolution of material structure and response from fabrication (e.g. welding) to in-service operation. Individual reviews for welding simulations [5], power plant steels [6, 7], welding of 9Cr steel [8] and constitutive modelling [9] may be consulted separately. The aim of this review is to demonstrate the modelling methodologies available that could be assembled to create a through-process modelling methodology with which to predict the structural integrity of power plant components.

There is a need for a modelling approach to life-prediction of power plant components. The life of components is typically inferred from the behaviour of test specimens. Many examples of design-for-life are shown in engineering textbooks, e.g. [10]. These methods are based on extensive libraries of test data. Plant components are designed to comply with various standards, such as R5 [11] or R6 [12], but these standards are generally somewhat conservative. For high-cycle fatigue applications, Zhu and Xuan [13] compared different design standards for pressure vessels and found that microstructure was not taken into account in several codes and that all were overly conservative. For example, the allowable stress amplitudes permitted by the standards ranged from 40% to 4.5% of the tested stress amplitudes for the same number of cycles to failure.

Larrosa et al. [14] identified several challenges to accurate assessment of fitness-for-service of pipe components, e.g. development of methods to address load-history effects, definition of reference strain for strain-based methods, the treatment of complicated geometries and loadings, measuring creep-crack initiation times, etc. Such challenges lead to conservative design of components in order to account for design unknowns. A through-process model could address the

issue of over-conservatism by modelling directly the constitutive behaviour throughout a welded joint and by predicting directly the life of different regions in the joint.

Threats to the structural integrity of power plant steel come from the new operating conditions necessary for efficient power generation. The first new operating condition is the move from steady-state, essentially constant power, base-load operation to transient, flexible-operation [15]. One reason for this change is that advances in real-time monitoring allow plant operators to adjust power output to suit demand. Another reason is the increased use of wind energy, e.g. a 20-fold increase in 15 years for some countries [16]. When energy demand is constant but wind-energy output fluctuates due to the variability of wind conditions, thermal power plant must intervene to a greater or lesser extent in order to match the energy demand.

Another challenge is the drive for cleaner power generation, often mandated by governments [17-20], through increased thermal efficiency of plant. This can be increased by operating plant at higher steam pressures and temperatures, as illustrated in Fig. 1. Flexible operation subjects power plant components to cyclic loading, while the drive for increased efficiency leads to more severe thermal and thermomechanical loading and early failure of plant components.

In order to address the new challenges facing power plant, a through-process modelling methodology for power plant steel is needed. This review will deal specifically with 9Cr steels. Section 2 describes 9Cr power plant steel and the weakening effect of the welding processes. Section 3 describes the first aspect of through-process modelling, namely the thermal modelling for welding. In a through-process model, the temperature history is used to predict microstructure evolution. Section 4 details various microstructure evolution models, with specific application to 9Cr steel. Section 5 describes constitutive modelling of plant components; these models are shown to be microstructure-dependent. Section 6 concludes the review with general commentary and future considerations for through-process modelling.

## 2. 9Cr steel

### 2.1: 'As-received' material

9Cr steels are alloys of chrome, molybdenum and vanadium, e.g. P91 and P92, with additional elements. Typical sample compositions of P91 and P92 are displayed in Tables 1 and 2, respectively. It is clear from Tables 1 and 2 that '9Cr' describes a range of steel alloys with varying compositions so that although two steel samples might nominally be the same steel, they may actually have significant differences in chemical composition. Such variance in composition is permitted by industrial standards, e.g. [21], but it may affect the formation of the 9Cr steel microstructure, e.g. the composition of carbide precipitates.

The microstructure of 9Cr steels is hierarchical, meaning that it has different microstructural features at different length-scales, e.g. grains at the largest scale and martensitic laths at the lowest. A lath is a dislocation sub-structure with high dislocation-density. The martensitic lath microstructure provides 9Cr steel with high-dislocation-density in the as-received state, although under long-term exposure to high-temperature, laths can evolve into sub-grains [8, 22, 23], which are typically less than 1  $\mu\text{m}$  in size. It is due to this hierarchical microstructure that 9Cr steels can maintain high strength at high temperatures.

In the as-received state, 9Cr steel has excellent high-temperature strength due to the high dislocation-density lath microstructure. However, dislocation-density can reduce via different mechanisms such as annihilation, locking and dipole-forming [24], all of which are associated with dislocation motion. To maintain material strength by preventing such mechanisms, the microstructure of 9Cr steel places obstacles in the paths of dislocations. The main obstacle types are as follow:

- High-angle grain boundaries (HAGBs): Dislocations travel along slip systems (crystallographic systems are described elsewhere [25-27]), which are controlled by the orientations of grains. When the mismatch angle between two systems is too steep, the dislocation is pinned at the boundary of the two systems. In 9Cr steel, laths have low-angle boundaries (LABs) [28] and provide significantly less pinning. A collection of laths form a block. A collection of blocks form

a packet and packets exist within the boundaries of prior-austenite grains (PAG) [28, 29]. The mismatch-angles between blocks, packets and grains are greater than 10 to 15° [30] and are defined as 'high-angle' boundaries. At high temperature, small grains are detrimental to 9Cr strength, even though they increase the number of HAGBs. Local high-dislocation-density at high-angle boundaries combined with cross-slip and dislocation-climb (made possible by thermal energy at high temperature) allow for more dislocation-annihilation at high-angle boundaries at high temperatures.

- Solute: Alloying elements, such as tungsten in P92 [31], form individual clusters of molecules that are relatively immobile and retard dislocation motion. Solutes tend to disperse randomly throughout the microstructure, thereby arresting the motion of dislocations before they can reach HAGBs.
- Carbide precipitates: Similar to solutes, carbide precipitates, such as MX and  $M_{23}C_6$  [23, 32], are also relatively immobile. The smaller MX precipitates tend to disperse throughout the 9Cr microstructure while the larger  $M_{23}C_6$  precipitates tend to form along grain, packet, block and lath boundaries [23, 33, 34], thereby providing obstacles to dislocation-motion even at low-angle boundaries.

9Cr steel microstructure is optimised for high-temperature service via carefully-controlled heat-treatment to provide optimum toughness and creep strength [35]. Heat treatment typically involves a normalising heat-treatment and a tempering heat-treatment, with some examples displayed in Table 3. It is clear from Table 3 that normalising is generally conducted between 1000°C and 1100°C and that tempering is conducted between 700°C and 800°C and is usually a longer heat treatment than normalising.

Normalising heats the material into the austenite region, where recrystallisation and grain growth can occur. The normalising process is intended to produce large austenite grains of approximately equal size throughout the steel. After normalising, the material is quenched back into the martensite phase. The newly-formed martensite has fine laths, high dislocation-density and few  $M_{23}C_6$  precipitates [32], which typically dissolve at temperatures associated with normalising. Tempering allows  $M_{23}C_6$  precipitates to form again and to grow, which increases precipitate-strengthening, while also reducing dislocation density, increasing the lath widths and improving ductility.

## 2.2: Effect of welding on 9Cr steel

Welding processes subject the steel to locally high temperatures and form heat-affected zones (HAZ). A schematic representation of HAZ is shown in Fig. 2. The HAZ is subdivided as follows:

- Coarse-grained HAZ (CGHAZ): The CGHAZ temperatures approximate those of normalising heat-treatment processes. The steel transforms fully to austenite and the  $M_{23}C_6$  precipitates dissolve. The austenite grains recrystallize and then grow, leading to coarse grains.
- Fine-grained HAZ (FGHAZ): The temperatures experienced in the FGHAZ are sufficient to fully transform the material to austenite and cause grain recrystallization but the material typically cools before grain growth can occur.  $M_{23}C_6$  precipitates do not dissolve and may coarsen due to high temperatures.
- Inter-critical HAZ (ICHAZ): This region partially transforms to austenite. Some regions recrystallise while the remaining martensite softens due to additional tempering. The additional tempering effects cause  $M_{23}C_6$  precipitates to coarsen.
- Over-tempered parent metal (OTPM): This region experiences tempering temperatures (700°C to 800°C), leading to tempering effects such as martensitic lath coarsening and precipitate coarsening. The temperatures are insufficient for phase transformation to occur.
- Unaffected parent metal (PM): This region is too far from the fusion line to experience high temperatures such as those associated with phase transformation or even tempering. The microstructure is unaffected by the welding process.

Local regions in the welded joint renormalized by the welding process and thus require tempering to recover their microstructure and to relieve residual stresses. Post-weld heat treatment (PWHT) is usually applied to a weld to temper newly-formed martensite regions and to grow precipitates in regions lacking them. In power plant, 9Cr steels often fail by a mechanism known as Type IV cracking [36]. Type IV cracks occur in the fine-grained region of the HAZ, whether FGHAZ [7] or ICHAZ [37] and is usually associated with creep but similar cracks have been observed under cyclic conditions [38]. The cracking occurs because material strengthening mechanisms are lost due to:

- Fine grains, which present more grain boundaries and more opportunities for dislocation cross-slip and annihilation.
- Regions lacking martensite because undissolved  $M_{23}C_6$  precipitates leave a shortage of carbon in the austenite with which to form martensite. Then, during PWHT, the remaining carbon is lost to additional precipitates, leaving ferrite, which is a softer material phase than martensite [39], instead of martensite [31, 40].
- Coarse carbides in the ICHAZ [37] with increased spacing that are less effective at pinning dislocations.

Structural integrity of power plant components can be improved by minimising the detrimental effects of welding described above via an optimised welding and PWHT protocol. Industrial standards permit variability in the welding process, e.g. joint preparation [41], welding heat input (via torch arc current) [42], preheat temperature [43] and PWHT temperature and hold-times [44]. Such variability leads to a number of combinations of welding process too prohibitive to investigate experimentally in order to find the ideal welding process for 9Cr steel that will best preserve its strengthening mechanisms. However, it is possible to simulate them with computational models.

### 3. Thermal modelling

In order to simulate the welding process in finite-element (FE) simulation, the interaction between the welding torch and the component to be welded must be represented accurately. This requires consideration of the local heat input from the weld torch, the formation of a weld bead and the heat transfer from the weld bead to the surrounding material. Accurate modelling of the welding process will produce more accurate predictions for microstructure (Section 5) and residual stress distributions.

Common FE packages used to model welding of steels are Abaqus [45], SYSWELD [46] and ANSYS [47-49], with some institutions using alternative packages such as Code\_Aster [50]. Plant components, e.g. welded pipes, can be modelled using 3D FE meshes but this is computationally expensive. Axisymmetric models are often used to reduce the size of the FE mesh. A comparison of different meshes and models is given in Table 4. It is assumed that the number of finite elements gives an indication of computational expense and simulation-time required to implement the welding simulation.

3D FE models can be used to produce geometries that are the most representative of power plant components and can, in principle, best reproduce the welding process. However, 3D models of large piping components will be computationally-expensive to run and require significant computer resources. Axisymmetric models are more convenient to simulate but they do not capture the effects of a weld-torch moving around the circumference of the pipe or starting or finishing its run, as occurs in real welding processes and in 3D simulations. Instead, axisymmetric models represent an idealised process in which the weld bead is applied all around the circumference at the same time. 3D effects, such as pipe-distortion [49], are typically not captured by axisymmetric models but the average results between 3D and axisymmetric simulations tend to be comparable, at least in terms of residual stress [51, 52].

The heat source, representing the welding torch, can be applied as a moving heat-source, e.g. the double-ellipsoid heat source model proposed by Goldak et al. [53]. This gives a 2D ellipsoidal or

3D double-ellipsoidal heating zone with its centre corresponding to the centre of the heat source. The model is described as follows in [51]:

$$Q(x', y', z') = \frac{6\sqrt{3}f_f Q_w}{a_1 b c \pi \sqrt{\pi}} \exp\left(-\frac{3x'^2}{a_1^2} - \frac{3y'^2}{b^2} - \frac{3z'^2}{c^2}\right) \quad (1)$$

$$Q(x', y', z') = \frac{6\sqrt{3}f_r Q_w}{a_2 b c \pi \sqrt{\pi}} \exp\left(-\frac{3x'^2}{a_2^2} - \frac{3y'^2}{b^2} - \frac{3z'^2}{c^2}\right) \quad (2)$$

$$Q_w = UI\eta \quad (3)$$

where  $x'$ ,  $y'$  and  $z'$  are the local coordinates of the double-ellipsoid. The material being welded may be a plate (Cartesian coordinates) or a pipe (polar coordinates), for example.  $Q_w$  is the welding power,  $U$  is the torch voltage,  $I$  is the torch current and  $\eta$  is the torch efficiency. The torch efficiency is typically from 50% to 100% [51, 54, 55].  $a_1$ ,  $a_2$ ,  $b$  and  $c$  are welding parameters which can be adjusted to give the desired weld pool.  $f_f$  and  $f_r$  describe the fractions of the heat source in front of and behind the torch and these fraction sum to a value of 2 [51], e.g. if the fractions of the heat source in front of and behind the torch balance then  $f_f = f_r = 1$ , so  $f_f + f_r = 2$ .

The moving heat source can be defined in general-purpose FE software, e.g. Abaqus, with a user-defined subroutine to control the path and speed of the torch. General-purpose FE software can be supplemented with additional software to increase the accuracy of the simulation, e.g. the weld-modelling tool FEAM-WT can be used in conjunction with Abaqus to help fit welding parameters [50]. The criterion for whether to use 2D or 3D ellipsoidal heat distributions is the Peclet number, although the value of this number below which 2D distributions are acceptable is not well defined [50]. SYSWELD is a dedicated welding model with such features as 2D and 3D heat distributions built-in [56]. Such dedicated welding software has been found to give superior temperature predictions compared to general-purpose software [50].

An alternative method for applying heat to geometry is a method known as 'element-birth', also called 'block-dumping'. This involves initially modelling all weld-bead elements in the FE geometry and then selectively activating them and applying a heat flux to them in order to raise their temperature [57]. The heat flux is defined using the net line energy of the weld, defined here as [45, 54]:

$$q = \frac{Q_w}{v} \quad (4)$$

where  $v$  is the weld torch traverse speed. The heat flux, sometimes called DFLUX, is then defined as follows [45]:

$$DFLUX = \frac{qv}{V} \quad (5)$$

where  $V$  is the volume over which the heat energy is applied.

As has been noted, 2D FE modelling of the welding process cannot capture 3D effects of welding, one of which is heat transfer along the welding travel direction. This can result in overestimation of the heat input in the 2D model when applying welding process parameters (Eqn. 4) from the real welding process to the FE geometry. Song et al. [58] proposed an analytical model to account for heat transfer in the weld travel direction in 2D models, which showed close agreement with the results of several separate real welding experiments.

It is also possible to specify temperature boundary conditions to elements to raise their temperature without reference to torch parameters [54]. In the case of block-dumping, it is possible to adjust the heat input to satisfy two criteria [45, 55]:

- All elements in the weld bead should exceed the melt temperature of the WM.
- The weld bead should produce a HAZ which is a reasonable distance from the fusion line.

In order to satisfy these criteria, the heat transfer mechanisms of conduction, convection and radiation within the geometry must be accurately modelled. Convection and radiation can be addressed separately [59] or can be combined into a single convection coefficient [45, 51, 55, 60, 61],  $h$ , as follows:

$$h = 0.0668T \quad 0 \leq T \leq 500^{\circ}\text{C} \quad (6)$$

$$h = 0.231T - 82.1 \quad T > 500^{\circ}\text{C} \quad (7)$$

where  $T$  is temperature, so the combined radiation-convection heat-transfer coefficient is temperature-dependent. It is also possible to use constant values [56, 57] rather than temperature-dependent terms. Heat-transfer mechanisms, e.g. conduction coefficients [45], can be derived from empirical data but there are limitations to this approach, e.g. modelling of heat transfer in the weld pool, where data is unavailable or difficult to measure or obtain.

In solid-mechanics simulations, liquid flow in the weld pool can be modelled by increasing the conductive properties, e.g. by doubling them [55], to represent more rapid heat transfer in the molten region. Another method is to model a liquid weld pool using computational fluid-dynamics (CFD) and then extract effective heat-transfer properties for use in the solid-mechanics simulation [48, 62]. The cellular-automata (CA) method can be used to model the weld pool [63] too but it requires constant re-meshing of the FE geometry as well as coupling between the CA grid and the FE mesh. CA is computationally expensive so that large weld pools should be avoided although this may not be possible for multi-pass welds of thick pipes.

Murthy et al. [59] showed that the residual stress results for a multi-pass welded pipe could be approximated by simulating only the final pass or the final six passes all at once. In order to accurately predict microstructure distribution in the weld, however, modelling only the final passes in a multi-pass simulation would lead to inaccurate results.

#### 4. Microstructure evolution model

##### 4.1. General

The temperature histories predicted by thermal models can be used to predict the material microstructure distribution, e.g. the location of different HAZ regions. In Section 2, several microstructure features were highlighted as important to the strength and performance of 9Cr steels. This section will explore some mathematical models used to predict the evolution of these different microstructure features, namely solid-state phases, austenite grain size, lath-width and precipitate size. The ability to accurately predict microstructure evolution, and thus the evolution of strengthening mechanisms, will enable more accurate prediction of in-service component performance and life.

##### 4.2. Phase transformation

During welding, 9Cr steel transforms from martensite to austenite and back again. Martensite-austenite transformation occurs rapidly and the transformed volume-fraction can be approximated as being directly proportional to the transformation temperature [64]:

$$\xi_{eq} = 1 - \frac{A_{c3} - T}{A_{c3} - A_{c1}} \quad (8)$$

where  $\xi_{eq}$  is the volume fraction of austenite at equilibrium. Non-linear martensite-austenite transformed volume-fractions can also be used [46]:

$$\frac{d\xi_{\gamma}}{dt} = \frac{\xi_{eq} - \xi_{\gamma}}{\tau(T)} f(\dot{T}) \quad (9)$$

where  $\xi_{\gamma}$  is the volume fraction of austenite. Under non-equilibrium conditions, such as welding, the austenite transformation temperatures may increase [65]. Composition-based empirical models [66], as well as software such as ThermoCalc [67], can be used to calculate transformation temperatures.

Observation of the 9Cr continuous-cooling-transformation (CCT) diagram shows that for all but the slowest cooling-rates (e.g. slower than 6°C/minute [66]), 9Cr austenite will only form martensite [68]. The austenite-martensite transformation is commonly described using the Koistinen-Marburger function [69], although linear rules have been used under the assumption of rapid transformation [39, 70]. Other methods of calculating the martensite volume fraction are described by Yu [71] and Huyen et al. [72].

Phase field modelling (PFM) [73, 74] is a physically-based approach to solid-state transformation. The general framework of PFM is that for any grain:

- A phase-field parameter will have a value of 1 inside the grain and a value of 0 outside of the grain.
- The interface between grains shall have interface mobilities, energies, thicknesses and driving pressures.
- The domain will have a spatial distribution of nucleation sites for grains, a density of nuclei and a nucleation temperature range.

Microstructure evolution occurs as the system attempts to minimize its free energy. A source of energy can include heat- and strain-energy. PFM can be coupled with thermodynamic simulation tools, such as ThermoCalc [75], to aid the identification of PFM parameters. Boettger et al. [76] assessed different methods of increasing the efficiency of such couplings. Despite the use of ThermoCalc or other software packages, a certain amount of parameter-fitting is still required for PFM, e.g. for the spacing of ferrite and bainite nuclei [75]. A drawback of PFM is the very small size-scale for which PFM is applicable, e.g. micro-scale (see Table 5). Comparing the PFM modelling domains in Table 5 to the FE geometries in Table 4, it is clear that it would be prohibitively expensive computationally to use PFM for simulation of real power plant component geometries.

#### 4.3 Austenite grain size

During welding, austenite grains recrystallize and then undergo further growth [77]. Further reading on recrystallization phenomena can be found in the review by Doherty et al. [78]. For 9Cr steel, packet-size and block-size can be linearly related to grain size [77, 79]. Examples of grain size evolution models are described by numerous authors [39, 64, 80-83]. The recrystallization term,  $S$ , can either be dependent on initial grain size,  $d_0$  [81]:

$$S = 1 - \exp\left[-\frac{K}{d_0} t^n\right] \quad (10)$$

or on a critical value of normalised dislocation-density,  $\bar{\rho}_c$  [80]:

$$\dot{S} = H[x\bar{\rho} - \bar{\rho}_c(1 - S)](1 - S)^{\lambda_1} \quad (11)$$

where  $K$ ,  $n$ ,  $H$ ,  $x$  and  $\lambda_1$  are all constants.  $\bar{\rho}_c$  is a critical value of normalised dislocation-density. Dislocation-density,  $\bar{\rho}$ , evolves during plastic deformation (see Section 5 below).

PAG-growth can be modelled using static (temperature and time dependent) and dynamic (temperature, time and plastic strain dependent) terms. Two examples are as follows:

$$\dot{d} = \frac{M\sigma_{surf}}{d\gamma_0} + \frac{\alpha\dot{\epsilon}_p}{d\gamma_1} \quad [81] \quad (12)$$

$$\dot{d} = G_1\left(\frac{d_0}{d}\right)^{\psi_1} - G_2\dot{S}\left(\frac{d}{d_0}\right)^{\psi_2} \quad [80] \quad (13)$$

where  $d$  is the PAG size and  $\gamma_0$ ,  $\gamma_1$ ,  $\alpha$ ,  $G_1$ ,  $G_2$ ,  $\psi_1$  and  $\psi_2$  are constants,  $\sigma_{surf}$  is the grain boundary energy per unit area and  $M$  is grain boundary mobility. Equation 12 includes recrystallization (the first term) and a dynamic, plasticity-driven grain-growth term (the second term) while Eqn. 13 has a static grain-growth term (the first term) and recrystallization is handled with a separate equation, e.g. Eqn. 10 or 11. Results from a model using Eqn. 13 are shown in Fig. 3, with close correlation achieved between test data and model.

Equations 12 and 13, as presented here, were applied in the context of hot-rolling and annealing of ferritic steel. These models would require modification before being applied to 9Cr steel. Hamelin et al. [39] applied a static grain-growth model in the context of welding of a nuclear power plant steel as follows:

$$d^4 - d_0^4 = 2.969 \times 10^{15} \sum \Delta t \cdot \exp\left(-\frac{69300}{T}\right) \quad (14)$$

where  $d$  and  $d_0$  represent the final and initial PAG sizes (mm) over time increment  $\Delta t$  at temperature  $T$  (K), respectively.

The Monte-Carlo (MC) method has been used to simulated grain size evolution in HAZ [84, 85] with high precision and but the simulation results of MC modelling depend on the grid size and spacing and on how the simulation time is coupled to real time. This introduces extra complexities that would be unwelcome in a through-process model of steels as complex as 9Cr steels. The geometries that can be simulated by MC methods are also small (0.24 mm × 6 mm × 2.4 mm [84]) or relatively small (33 mm × 8 mm × 3 mm [85]) compared to component-scale geometries. Some HAZ grain evolution predictions using MC are shown in Fig. 4. In Fig. 4, it is clear that the slowest torch speed, and therefore the longest exposure to high temperature, led to the most significant grain-growth, as expected. Despite the accuracy of MC, it, like PFM, is too computationally expensive to be practical for use on macro-scale models.

#### 4.4 Lath width

Lath-width is an important consideration in 9Cr steel. The laths are the lowest level of the hierarchical microstructure they serve as an indicator of dislocation-density, which has already been identified as vital to 9Cr strength (see Section 2). During welding, laths disappear from the material during transformation into the austenite phase. After welding, newly-formed martensite regions in the HAZ have fine laths and high dislocation-density. One of the key microstructural changes that occur during PWHT is that laths coarsen. A through-process modelling approach should therefore include the evolution of lath-width.

Galindo-Navo et al. [79] showed a microstructural model that can predict the size of martensitic laths,  $w$ , and their evolution during tempering:

$$w = w_0 + \lambda_0 x_c^{\alpha'} \sqrt{D_{diff} t} \quad (15)$$

where  $D_{diff}$  is carbon diffusion rate,  $w_0$  is initial lath width,  $x_c^{\alpha'}$  is carbon atom content in the martensite,  $\lambda_0$  represents a resistance to carbon diffusion and  $t$  is tempering time. This lath-width model almost exclusively uses measurable, physical parameters and reduces the necessity for fitting parameters. Some results from this model work are shown in Fig. 5. In Fig. 5, it is clear that the relationship between the carbon content and lath-widths of a variety of steels is well-represented by the model.

An alternative way to model lath widths and their evolution is to relate the widths to low-angle boundary dislocation-density evolution [86]:

$$w = \frac{w_0 \rho_{w,0}}{\rho_w} \quad (16)$$

where  $\rho_{w,0}$  is initial dislocation-density at the low-angle boundary and  $\rho_w$  is current low-angle-boundary dislocation-density.

Lath-width evolution can also be modelled directly from ageing test data (e.g. [87]) or creep data (e.g. [23]), which is pertinent to the long-term, in-service aspect of structural integrity prediction. Such an equation may take the form of an Otswald-ripening model:

$$\dot{w} = \frac{a}{w^m} \quad (17)$$

where  $a$  is a constant coefficient and the exponent  $m$  typically has a value greater than 2.

#### 4.5 Carbide precipitate size

At high temperatures, carbides dissolve and disappear from the material microstructure. Tempering allows the carbides to precipitate out of solution and increases the precipitate-strengthening effect of the microstructure.

Myhr and co-workers [88-91] suggested a precipitate evolution model for aluminium alloys. Despite the nano-scale nature of these models, they were applied to macro-scale geometries. Figure 6 shows a comparison of predicted and measured mean particle radius and number density of precipitates in an Mg-Si alloy. It is clear from Fig. 6 that the quantitative and qualitative trends of the experimental data were captured by the model.

An alternative modelling method is described by Lin et al. [81] to represent how precipitates dissolve at high temperature:

$$\dot{P} = Dy \left( \frac{L - y}{L} \right) \quad (18)$$

where  $\dot{P}$  is the rate of decrease in population of precipitates,  $L$  is the sustainable population of precipitates,  $y$  is the population size factor (or the viable concentration of precipitates [92]) and

$$D = D_0 \exp \left( -\frac{Q}{RT} \right) \quad (19)$$

where  $D_0$  is the diffusion coefficient,  $Q$  is an activation energy and  $R$  is the universal gas constant.

Precipitate growth, e.g. during PWHT, can be described with an Ostwald-ripening-type equation [93]:

$$d_{p,t}^n - d_{p,0}^n = kt \quad (20)$$

where  $d_{p,t}$  is precipitate size at time  $t$  at a certain temperature,  $d_{p,0}$  is the initial precipitate size and  $k$  is a temperature-dependent growth coefficient. A similar equation can be used to describe the growth of MX precipitates and Laves phase [94].  $k$  can be described as follows [93]:

$$k = k_0 \exp \left( -\frac{Q}{RT} \right) \quad (21)$$

or another example of  $k$  for a maraging steel [95] is as follows:

$$k = \frac{8\gamma_p V_m D_p x_{j,p}}{9RT} \quad (22)$$

where  $x_{j,p}$  is the volume of element  $j$  as it goes from the matrix into precipitate,  $D_p$  is the diffusion coefficient,  $V_m$  is particle molar fraction and  $\gamma_p$  is the interfacial energy. Precipitate size can also be modelled with a strain-rate dependency in 9Cr steel using a modified Ostwald ripening law [96].

The strengthening mechanism of precipitates is not determined solely by their diameter. In fact, precipitate spacing and volume fraction are two additional considerations. The volume fraction determines the degree to which the material is saturated with precipitates. With increased volume fraction, there is increased dislocation-pinning due to the precipitates, although the material as a whole will be softer due to the additional tempering necessary to increase the volume fraction. As precipitates form during tempering, carbon is removed from the martensite matrix, leading to a softer material [97].

For a given volume fraction of precipitates, the dislocation-pinning effect is determined by the precipitate spacing. Precipitate spacing can be determined from precipitate diameter for a constant volume fraction,  $V$ , as follows [98]:

$$\lambda = d \left( \frac{\pi}{6V} \right)^{1/3} \quad (23)$$

It is clear that microstructure models can be physically-based to a greater or lesser extent. The work of Galindo-Nava, for example, is highly physically-based whereas other authors have used more empirical approaches with fitting-parameters, e.g. [99]. The ability to predict microstructure evolution with precision is important in the context of physically-based constitutive modelling.

## 5. Structural model

### 5.1 General

Damage modelling and life prediction for power plant components are strongly dependent on constitutive response of the material, whether by fatigue-life estimates [100], crack-growth dynamics [101, 102] or creep-life estimates [103]. The constitutive behaviour of welded components depends on (a) the thermal history of the material during welding, (b) the material microstructure and (c) the in-service loading conditions. As power plant moves from base-load to flexible operation, welded components are subjected to combined-loading (e.g. creep-fatigue rather than just creep) so it is important that constitutive models be capable of predicting material response for a range of loading conditions.

Welding analysis typically utilises uncoupled thermal and mechanical analyses [45, 46, 49, 54, 61]. The thermal analysis is performed on FE geometry without reference to mechanical properties

and is purely a heat-transfer analysis. A sequential mechanical FE model can be prepared with an identical geometry and mesh so that the temperature history extracted from the thermal analysis can be applied node-for-node as a thermal load. The thermal load generates strain in the mechanical model. The general set of strains is often described as follows [39]:

$$\varepsilon = \varepsilon^e + \varepsilon^p + \varepsilon^{th} + \varepsilon^{tr} + \varepsilon^{tp} \quad (24)$$

where the strain components are elastic, plastic, thermal, metallurgical and transformation-induced plasticity (TRIP), respectively. Thermal strain occurs due to thermal expansion, metallurgical strain occurs when phase transformation causes volume change [6, 39] and TRIP occurs in 9Cr steel during martensitic transformation [6].

TRIP is typically only modelled for martensitic transformation because it occurs at lower temperatures when the resulting stresses are larger in magnitude. Some authors have eliminated plastic strains and material hardening history at high temperatures in an ‘annealing’ process [54, 104, 105], leaving only the effects of strains at lower temperatures. One modelling method to capture TRIP is to reduce the material yield stress during martensitic transformation to ensure yielding and plasticity [61]. For an elastic-perfectly plastic material, Leblond et al. [106] suggested the following model for calculating TRIP:

$$\dot{\varepsilon}_{TRIP} = \frac{3}{2} \frac{(\varepsilon_{\alpha}^{th} - \varepsilon_{\gamma}^{th})}{\sigma_{\gamma}^y} h \left( \frac{\sigma_{eq}}{\sigma_{mix}^y} \right) \sigma(\ln \xi_m) \xi_m \quad (25)$$

$$h \left( \frac{\sigma_{eq}}{\sigma_{mix}^y} \right) = 1 \quad \frac{\sigma_{eq}}{\sigma_{mix}^y} \leq \frac{1}{2} \quad (26)$$

$$h \left( \frac{\sigma_{eq}}{\sigma_{mix}^y} \right) = 1 + \frac{7}{2} \left( \frac{\sigma_{eq}}{\sigma_{mix}^y} - \frac{1}{2} \right) \quad \frac{\sigma_{eq}}{\sigma_{mix}^y} > \frac{1}{2} \quad (27)$$

$$\sigma_{mix}^y = [1 - f(\xi_{\alpha})] \sigma_{\gamma}^y + f(\xi_{\alpha}) \sigma_{\alpha}^y \quad (28)$$

$$\sigma_{\alpha}^y = \xi_L \sigma_L^y + \xi_U \sigma_U^y \quad (29)$$

where  $\sigma_{\gamma}^y$  is the yield stress of austenite and  $\sigma_{\alpha}^y$  is the yield stress of martensite, using a rule-of-mixtures between tempered and newly-formed martensite yield stresses  $\sigma_L^y$ ,  $\sigma_U^y$ , with volume fractions  $\xi_L$ ,  $\xi_U$ . This model considers the instantaneous volume fraction of phases while another model incorporates the rate of change of volume fraction [107], described by Hamelin et al. [39] as:

$$\dot{\varepsilon}^{tp} = \frac{3}{2} K s f'(z) \dot{z} \quad (30)$$

where  $K$  is a material constant,  $s$  is the deviatoric stress tensor during transformation and  $z$  is the phase volume fraction. This formulation is presented in multi-axial form. TRIP can also be modelled via a micromechanics approach [108] with extrapolation of the cumulative local material responses to predict the macroscale material behaviour.

An alternative method of accounting for TRIP directly is to consider the differential coefficients of expansion of the martensite and austenite phases [60]. During heating and cooling, differential expansion and contraction rates for adjacent regions of differing material phases will lead to strain incompatibilities with resultant elevated stress and plasticity. It is also possible to ensure plasticity by defining the material yield stress to be reduced during the transformation process [61].

## 5.2 Phenomenological continuum mechanics modelling

Phenomenological models are typically constructed using parameters and coefficients identified from material test data rather than relying on physical material parameters, e.g. microstructure features. For the purposes of the welding simulation, material behaviour can be determined from tensile monotonic data as opposed to long-term creep data, for example. The accuracy of such fitting is sensitive to the test data. For example, the maximum strain from a tensile test [104] affects what stress-strain data is available for parameter identification. When cyclic data is used to fit the kinematic hardening parameters, the saturated cyclic response is typically used [104], so that models calibrated against tensile or cyclic data for the same material will not predict the same stress-strain responses.

9Cr steels harden kinematically and cyclically soften isotropically [28, 29, 109, 110]. Although it may be sufficient to model the material as perfectly-plastic for the purposes of welding [46], this

would predict unrepresentative stress-strain responses during in-service loading. Chaboche reviewed a number of plasticity theories [9], including the Armstrong-Frederick model for non-linear kinematic hardening:

$$\dot{\mathbf{X}} = \frac{2}{3} C \dot{\boldsymbol{\varepsilon}}_p - \gamma \mathbf{X} \dot{p} \quad (31)$$

where parameters in bold indicate tensors. The parameter  $C$ , called hardening modulus, represents the initial hardening slope, and the rate-of-decay constant,  $\gamma$  controls the rate of reduction of the kinematic hardening slope;  $p$  is equivalent plastic strain [25]. This model describes hardening which saturates at a maximum value  $C/\gamma$ . Multiple back-stress terms can be used to achieve a more accurate fit to short- and long-strain-range test data. Additional terms can also be included to take account of dynamic and static recovery, as well as threshold values (values of the magnitude of  $\mathbf{X}$ , below which only the first term in Eqn. 31 is used) can be defined too. For this non-linear model, each back-stress requires two fitted parameters.

Non-linear isotropic cyclic softening (or hardening), referred to as the Chaboche model, is commonly described as follows:

$$\dot{R} = b(Q - R)\dot{p} \quad (32)$$

where  $R$  is the isotropic variable,  $Q$  defines the asymptotic value of hardening (or softening, with a negative  $Q$ -value) towards which  $R$  saturates.  $b$  controls the rate at which  $R$  reaches a value of  $Q$ . As with kinematic hardening, multiple isotropic terms can be used to achieve increased accuracy of fitting to test data.

Chaboche compared several viscoplastic models [9] and all were found to give similar results between plastic strain-rates of  $1 \times 10^{-8} \text{s}^{-1}$  and  $1 \times 10^{-4} \text{s}^{-1}$ . All except one (the Bodner model, which had directional hardening without using kinematic backstress,  $\mathbf{X}$ ) of the models gave similar results up to about  $0.03 \text{s}^{-1}$ . 9Cr steels are visco-plastic at high temperature, such as at power plant operating temperatures, so that the stress-strain response is strain-rate dependent [111].

Visco-plastic behaviour can be represented with a power-law function [80] or a hyperbolic sine function [29, 109]. The hyperbolic sine function is a non-linear term when plotted on log-log graphs, so it can better capture the visco-plasticity behaviour of 9Cr steel than a single power-law equation (see Fig. 7). Multiple power law functions can be used but they increase the number of modelling parameters required and have less fidelity to the visco-plastic deformation mechanisms, e.g. diffusion or dislocation mechanisms [112, 113].

Constitutive models, whether incorporating kinematic hardening, isotropic softening or elastic perfectly plastic, are used to predict welding residual stress in the welded joint. PWHT is used to relieve residual stresses as well as to recover material microstructure. Section 4 described various methods by which to model the evolution of microstructure. Stress relaxation during PWHT can be modelled by introducing time-dependent modifications, which soften the material, to the kinematic and isotropic hardening terms [114]. Benaarbia et al. [115] accounted for relaxation effects using visco-elastic terms in their material model. Stress-relaxation, assuming no applied strain ( $\dot{\boldsymbol{\varepsilon}}_{Total} = 0$ ), can also be modelled by inverting creep models [116].

For in-service operation, all three models (kinematic hardening, cyclic softening and creep) can be used, e.g. [117]. With sufficient test data from a variety of tests and test conditions, a complete constitutive model can be assembled for welding, PWHT and in-service operation of 9Cr steel components.

As discussed in Section 2 and shown in Fig. 2, welding modifies the local microstructure to form a HAZ. From one region in the HAZ to the next, there are gradients in microstructure and consequently in constitutive behaviour, e.g. harder and softer regions due to gradients in dislocation-density. The HAZ presents a challenge to through-process modelling using phenomenological methods. The HAZ can be taken as a single material region [118, 119] (Fig. 8a), or as multiple sub-regions [111] (Fig. 8b). Hall et al. [120] modelled welded connections using a four-material model while Hayhurst et al. [121, 122] used a five-material model. Increased HAZ subdivision requires increased numbers of modelling parameters and associated testing for identification.

HAZ material parameters can be identified by testing cross-weld, parent metal and weld metal specimens and by applying PM and WM parameters to a 3-material FE geometry and fitting the HAZ parameters [119]. It is also possible to heat-treat parent metal to achieve a microstructure representative of a particular HAZ region, e.g. the ICHAZ, and identify material parameters from test data pertaining to that material [123]. Alternatively, cross-weld specimens may be tested using digital imaging correlation (DIC), to observe the local constitutive behaviour of HAZ regions for parameter identification [111]. A key challenge with these methods is the assumption of a discrete HAZ sub-region with its own particular constitutive behaviour when in fact there is a continuous gradient of material microstructure and behaviour. Such an assumption is unavoidable because it is impractical to keep sub-dividing the HAZ into smaller and smaller regions and identify parameters for them but the assumption results in a reduction in the accuracy of the model.

PWHT also changes mechanical behaviour [34, 77, 93, 124-127], in effect producing a new material needing even more modelling parameters. An alternative to the phenomenological model is the physically-based model.

### 5.3 Physically-based continuum mechanics modelling

In principle, physically-based models require fewer tests for calibration but instead require measurement or knowledge of physical parameters such as the microstructural features mentioned in Section 4. Measurement of microstructural parameters constantly becomes more practical with improvements in instrumentation and methodologies for microscopy such as scanning electron microscopy [128], transmission electron microscopy [129], energy-dispersive X-ray spectroscopy [67], electron backscatter diffraction [130], etc. Knowledge of how microstructure affects constitutive behaviour can avoid the phenomenological model challenge of requiring large quantities of data to fully characterise a welded connection.

Different microstructural features influence the yield stress, from the alloying elements [131], the precipitates [90], solutes [95], martensitic block size [95, 132] and dislocation density [132]. Barrett et al. [3] recently proposed a physically-based yield stress model for 9Cr steels that incorporated solid solution-, precipitate- and PAG boundary-strengthening. Figure 9 shows a variety of yield stresses predicted from a dislocation-density model [132] compared to a variety of yield stresses from test data. The utility of a physically-based yield stress model is clearly demonstrated by achieving close correlation with test data despite the diversity of steels considered.

Kinematic back-stress can have different physically-based components, such as lath-boundary strengthening [28] as well as precipitate-, HAGB- and dislocation-substructure-strengthening [86]. Sauzay et al. [28] developed a lath-boundary back-stress model as follows:

$$x = x_0 + \frac{\mu}{1 - \nu} \sqrt{\frac{0.45\theta}{2\pi}} \frac{1}{\sqrt{w/b}} \quad (33)$$

where  $x$  is the kinematic back-stress,  $x_0$  is a stress parameter without considering lath-boundary effects,  $\mu$  is shear modulus,  $\nu$  is Poisson's ratio,  $\theta$  is angle of mis-orientation between laths,  $w$  is the lath-width and  $b$  is the magnitude of the Burgers vector. This particular model, based only on measurable material parameters, was successfully applied to model the cyclic softening via reduction in back-stress of P91 at 550°C.

Isotropic hardening can similarly be physically-based [133], e.g. using Taylor hardening:

$$R = \alpha\mu b\sqrt{\rho} \quad (34)$$

where  $\alpha$  is a constant and  $\rho$  is the dislocation-density. Again, these parameters are measurable rather than fitted.

Dislocation-density, which can be treated as a dimensionless, normalised parameter [80, 82], or as a true value, evolves according to temperature and plastic strain [133]. Test data suggests a strong correlation between lath width and dislocation-density ( $R^2 > 0.99$ ) under creep conditions [23] and a variety of physically-based dislocation-density evolution models have been adopted [24, 132, 134].

Some results from dislocation-density based models are shown in Fig. 10. In Fig. 10a, the dislocation-density model shows close correspondence with the 9Cr steel test data at a room temperature and high-temperature, with and without prior cold-working. Fig. 10b shows close correspondence between the model and aluminium test data for repeated groove pressing processes.

It is clear that there are physically-based alternatives to the kinematic hardening and isotropic softening models of Section 5.2. Physically-based creep models, which could be used for PWHT stress-relaxation, have also been proposed, e.g. [135] and [136], based on the Hayhurst model [121]:

$$\dot{\epsilon}_{cr} = \dot{\epsilon}_0 \exp\left(-\frac{\Delta F}{k_B T}\right) \sinh\left(\frac{\sigma(1-H)}{\sigma_0(1-D_p)(1-D_{cr})}\right) \quad (35)$$

where  $\Delta F$  is Helmholtz free energy,  $k_B$  is Stefan-Boltzman constant,  $H$  is continuum damage mechanics (CDM) primary hardening parameter and  $D_{cr}$  is CDM intergranular cavitation parameter.  $\sigma_0$  and  $D_p$  are described as:

$$\sigma_0 = \frac{M k_B T}{b^2 \lambda_{ob}} \quad (36)$$

$$D_p = 1 - \frac{\lambda_0}{\lambda} \quad (37)$$

where  $M$  is the Taylor factor,  $\lambda_{ob}$  is obstacle ( $M_{23}C_6$  and MX precipitates, dislocations and high- and low-angle boundaries) spacing,  $\lambda_0$  is initial mean obstacle spacing and  $\lambda$  is current obstacle spacing. This model included some fitting parameters (e.g. pertaining to  $D_{cr}$ ) but its physical basis allowed prediction of the detrimental effect of aluminium content on creep life in Bar 257 compared to P91 at two different temperatures (Fig. 11).

Comparing the phenomenological and physically-based constitutive models, it is clear that since physically-based models use microstructural parameters as inputs, the need for separate material parameters for each region in the HAZ, for each welding and PWHT process, is reduced.

#### 5.4 Microstructural crystal plasticity modelling

The modelling approaches described so far operate at the macro-scale. Macro-scale models assume that the material is isotropic and that its response is homogeneous. Of course, individual grains and laths behave anisotropically depending on orientation and geometry, leading to microscale inhomogeneous local stress-strain responses that may significantly affect macro-scale constitutive behaviour. Crystal plasticity (CP) models, e.g. [30, 137-139] can capture the interactions between, for example, grains of different sizes and of different orientations [138] and for 9Cr steel in particular, CP modelling has demonstrated the detrimental effect of precipitate-coarsening on fatigue life at 600°C [140], as well as the detrimental effect of small amounts of ferrite in the ICHAZ [141]. Despite such benefits, CP modelling has mainly been applied to FE geometries of limited size, e.g. a representative domain size of 176 x 111  $\mu\text{m}^2$  [140, 142], micro-scale cardiovascular stent struts [26] or micro-scale sub-models of compact-tension specimens [30].

Due to the micro-scale aspect of CP modelling, it may be possible to capture the material response in regions of steep microstructure-gradient such as the HAZ or to physically model the formation of cracks. This is highly attractive in terms of predicting component life but the small scale at which CP modelling operates makes it difficult to incorporate effects such as heat input from remote (e.g. several mm away) weld beads or stress redistribution from remote material locations to the area of interest during PWHT, for example. In the context of through-process modelling on component-scale geometries, e.g. pipe girth-welds [61, 143] or pipe saddle joints [119], CP modelling is currently too high-resolution and too computationally expensive to be practical. Similarly, coupled PFM-CP models are limited by small FE domains, e.g. 50 x 50 x 50  $\mu\text{m}^3$  [144].

Multi-scale methods [145-147] have been attempted in order to apply micro-scale models to macro-scale geometries but these require homogenisation techniques (e.g. varying the dimensions of laths but assuming that all laths are identical [140]) in order to reduce the complexity of the analyses, even though the macro-scale geometries are still relatively small compared to power plant

components. Some homogenisation techniques have also been shown to affect the predicted material response, e.g. monotonic stress increasing at higher strains without homogenisation compared to maintaining a consistent flow stress with homogenisation [148].

### *5.5. Structural integrity prediction*

A key factor in the structural integrity of welded components is residual stress. Residual stresses will contribute to the applied loading state of welded components and may result in premature failure even for nominally light loading applications. Tensile residual stress, in particular, is a concern since it is associated with accelerated crack growth [102]. Accurate prediction of residual stress states is therefore a necessary step in the through-process methodology. Such predictions can be used to determine if and how much PWHT is necessary following welding.

Figures 12 to 14 show a variety of residual stress comparisons between FE modelling and test data from different authors [58, 149, 150]. In each case, a continuum mechanics phenomenological model was implemented to predict the welding residual stresses. Young's moduli, yield stresses and hardening moduli were identified at a range of temperatures from test data and applied as temperature-dependent modelling parameters.

It is clear that reasonably accurate predictions of residual stress are possible using through-process modelling. This, combined with the microstructure evolution models discussed previously, should enable (future) more accurate predictions of the weld-region microstructure, which together with physically-based continuum structural models, should, in turn, facilitate more accurate predictions of in-service performance of welded components, e.g. along the lines of recent work by Mac Ardghail et al. [99].

### *5.6 Component life prediction*

Ultimately, the purpose of the constitutive modelling in the context of a through-process model is to predict effects of manufacturing processes on in-service component life but it is computationally expensive to simulate years of in-service loading in power plant. To predict long-term component-failure, approximate methods have been used, e.g. a strain-based fatigue indicator parameter [142], the Ostregren method [117, 151], a ratchetting-strain based damage indicator parameter [119]. For base-load operation, the Monkman-Grant correlation [152] can be used. Rouse et al. [103] noted that the failure time of components under creep could be predicted by integrating damage evolution models with respect to time. Barrett et al. [153] compared Coffin-Manson, Ostregren and Zamrik models to isothermal and thermos-mechanical fatigue (TMF) cyclic test data for P91 and found that the Zamrik model best predict TMF life.

Efficient alternatives to FE analysis, e.g. neural networks and Green's functions [154] or welding process parameter optimisation frameworks [155], could potentially also be adopted to increase the efficiency of computation. Therefore, structural integrity prediction using through-process modelling concepts is possible without the need for very long, computationally expensive simulations.

## **6. Conclusions:**

Prediction of component performance is only as reliable as the information available about the material, e.g. its microstructure and its residual stress state. To comprehensively measure these parameters in a welded component, if even possible, e.g. for ICHAZ regions due to their small size-scale, would typically be prohibitively expensive and, in the case of destructive testing, requires the fabrication of new components for actual use in power plant. If the microstructure and residual stress state could be accurately predicted based on knowledge of the as-received material and the welding and PWHT processes applied to it, then significantly more cost-effective life prediction would be possible. A through-process model represents the most complete way of accounting for changes to the as-received material due to welding and PWHT. There is, therefore, a need for a through-process modelling methodology for welded plant components in order to (a) make realistic and accurate life

predictions for next generation power plant components and (b) to identify the welding and PWHT processes that provide optimal in-service life, particularly in the drive to maximise plant efficiency and flexibility.

The current work focused on 9Cr steel components but the aspects of through-process modelling reviewed here could be extended to other power plant steels and indeed to other steel pipeline applications, e.g. oil and gas pipelines. Key conclusions from the present work are:

- Appropriate welding, microstructure evolution and constitutive models exist to construct a through-process modelling framework for 9Cr steel power plant components.
- Micro-scale models, such as phase field modelling, cellular automata, Monte Carlo methods and crystal plasticity modelling are highly accurate but are currently only practical for small geometries, not yet at the size-scales required for representing key power plant components. Macro-scale modelling is the most practical approach at present.
- Macro-scale, phenomenological constitutive models are sensitive to the test data from which their parameters are derived and the multi-material nature of the HAZ can quickly lead to a large number of modelling parameters.
- Macro-scale, physically-based constitutive models reduce the need for fitting parameters and material testing, thereby increasing precision and reducing cost. Modern instrumentation techniques make it feasible to measure microstructure parameters for use in physically-based models.

Despite the range of thermal welding, microstructure evolution and constitutive models available to researchers and designers, the authors are not aware of any attempts to combine and apply them as full through-process models, either to simple geometries or to power plant components. Further development of through-process modelling is therefore needed such as:

- Wider application of through-process methodologies optimisation of such approaches.
- Validation against test data for simple cases, e.g. high temperature low-cycle fatigue [64].
- Validation against operational data for power plant components.

## **7. Acknowledgements:**

This research is funded by Science Foundation Ireland grant numbers SFI/14/IA/2604 and supported in part by SFI/16/RC/3872. The authors would like to acknowledge the contributors to this research from GE Power (UK), ESB Energy International, University of Limerick, Imperial College, London, and Fraunhofer IWM, Freiburg.

## 8. References:

1. Wen, S.W., Hilton, P., Farrugia, D. C. J., *Finite element modelling of a submerged arc welding process*. Journal of Materials Processing Technology, 2001. **119**: p. 203-209.
2. Abburi Venkata, K., Kumar, S., Dey, H. C., Smith, D. J., Bouchard, P. J., Truman, C. E., *Study on the Effect of Post Weld Heat Treatment Parameters on the Relaxation of Welding Residual Stresses in Electron Beam Welded P91 Steel Plates*. Procedia Engineering, 2014. **86**: p. 223-233.
3. Barrett, R.A., O'Donoghue, P. E., Leen, S. B., *A physically-based high-temperature yield strength model for 9Cr steels*. Materials Science and Engineering A, 2018. **730**: p. 410-424.
4. Bhaskar, M.S., *Quantitative phase field modelling of precipitate coarsening in Ni-Al-Mo alloys*. Computational Materials Science, 2018. **146**: p. 102-111.
5. Lindgren, L.E., *Numerical modelling of welding*. Computer Methods in Applied Mechanics and Engineering, 2006. **195**: p. 6710-6736.
6. Francis, J.A., Bhadeshia, H. K. D. H., Withers, P. J., *Welding residual stresses in ferritic power plant steels*. Materials Science and Technology, 2007. **23**(9): p. 1009-1020.
7. Francis, J.A., Mazur, W., Bhadeshia, H. K. D. H., *Type IV cracking in ferritic power plant steels*. Materials Science and Technology, 2006. **22**(12): p. 1387-1395.
8. Pandey, C., Mahapatra, M. M., Kumar, P., Saini, N., *Some studies on P91 steel and their weldments*. Journal of Alloys and Compounds, 2018. **743**: p. 332-364.
9. Chaboche, J.L., *A review of some plasticity and viscoplasticity constitutive theories*. International Journal of Plasticity, 2008. **24**: p. 1642-1693.
10. Budynas, R.G., Nisbett, J. K., *Shigley's Mechanical Engineering Design, 9th Edition* 2011: McGraw-Hill.
11. *R5 Issue 3: Assessment Procedure for the High Temperature Response of Structures, EDF Energy, Gloucester, UK, 2014 Revision 002*.
12. *R6 Revision 4: Assessment of the Integrity of Structures Containing Defects, EDF Energy, Gloucester, UK, 2015 Amendment 11*.
13. Zhu, M.-L., Xuan, F.-Z., *Failure mechanisms and fatigue strength reduction factor of a Cr-Ni-Mo-V steel welded joint up to ultra-long life regime*. MATEC Web of Conferences, 2018. **165**.
14. Larrosa, N.O., Ainsworth, R. A., Akid, R., Budden, P. J., Davies, C. M., Hadley, I., Tice, D. R., Turnbull, A., Zhou, S., *'Mind the gap' in fitness-for-service assessment procedures-review and summary of a recent workshop*. International Journal of Pressure Vessels and Piping, 2017. **158**: p. 1-19.
15. Dong, Y., Jiang, X., Liang, Z., Yuan, J., *Coal power flexibility, energy efficiency and pollutant emissions implications in China: A plant-level analysis based on case units*. Resources, Conservation & Recycling, 2018. **134**: p. 184-195.
16. Sustainable Energy Authority of Ireland, *Energy in Ireland 1990 - 2015, 2016 Report*, 2016.
17. European Commission, *A policy framework for climate and energy in the period 2020 to 2030*. Communication from the Commission to the European Parliament, the Council, the European Economic and Social Committee and the Committee of the Regions, 2014.
18. European Commission, *A Roadmap for moving to a competitive low carbon economy in 2050*. Communication from the Commission to the European Parliament, the Council, the European Economic and Social Committee and the Committee of the Regions, 2011.
19. European Commission, *Analysis of options to move beyond 20% greenhouse gas emission reductions and assessing the risk of carbon leakage*. Communication from the Commission to the European Parliament, the Council, the European Economic and Social Committee and the Committee of the Regions, 2010.
20. Official Journal of the European Union, 2010. **L 290**: p. 39-48.
21. *I.S. EN 101216-2:2013*. The International Organisation for Standardisation, 2013.

22. Fournier, B., Sauzay, M., Renault, A., Pineau, A., Barcelo, F., Pineau, A., *Microstructural evolutions and cyclic softening of 9%Cr martensitic steels*. Journal of Nuclear Materials, 2009. **386-388**: p. 71-74.
23. Ennis, P.J., Czyrska-Filemonowicz, A., *Recent Advances in Creep Resistant Steels for Power Plant Applications*. Operation Maintenance and Materials Issue, 2002. **1**(1).
24. Hosseini, E., Kazeminezhad, M., *A new microstructure model based on dislocation generation and consumption mechanisms through severe plastic deformation*. Computational Materials Science, 2011. **50**: p. 1123-1135.
25. Dunne, F., Petrinic, N., *Introduction to Computational Plasticity*, 2005: Oxford University Press.
26. Sweeney, C.A., O'Brien, B., Dunne, F. P. E., McHugh, P. E., Leen, S. B., *Strain-gradient modelling of grain size effects on fatigue of Cocr alloy*. Acta Materialia, 2014. **78**: p. 341-353.
27. Inoue, I., Sadeghi, A., Koseki, T., *Slip band formation at free surface of lath martensite in low carbon steel*. Acta Materialia, 2019. **165**: p. 129-141.
28. Sauzay, M., Brillet, H., Monnet, I., Mottot, M., Barcelo, F., Fournier, B., Pineau, A., *Cyclically induced softening due to low-angle boundary annihilation in a martensitic steel*. Materials Science and Engineering A, 2005. **400-401**: p. 241-244.
29. Fournier, B., Sauzay, M., Pineau, A., *Micromechanical model of the high temperature cyclic behaviour of 9-12%Cr martensitic steels*. International Journal of Plasticity, 2011. **27**: p. 1803-1816.
30. Golden, B.J., Li, D-F., Guo, Y., Tiernan, P., Leen, S. B., O'Dowd, N. P., *Microscale deformation of a tempered martensitic ferritic steel: Modelling and experimental study of grain and sub-grain interactions*. Journal of Mechanics and Physics of Solids, 2016. **86**: p. 42-52.
31. Xue, W., Qian-gang, P., Yao-yao, R., Wei, S., Hui-qiang, Z., Hong, L., *Microstructure and type IV cracking behaviour of HAZ in P92 steel weldment*. Materials Science and Engineering A, 2012. **552**: p. 493-501.
32. Hurtado-Norena, C., Danón, C. A., Luppó, M. I., Bruzzoni, P., *Evolution of Minor Phases in a P91 Steel Normalized and Tempered at Different Temperatures*. Procedia Materials Science, 2015. **8**: p. 1089-1098.
33. Divya, M., Das, C. R., Albert, S. K., Goyal, S., Ganesh, P., Kaul, R., Swaminathan, J., Murty, B. S., Kukreja, L. M., Bhaduri, A. K., *Influence of welding process on Type IV cracking behaviour of P91 steel*. Materials Science and Engineering A, 2014. **613**: p. 148-158.
34. Pandey, C., Giri, A., Mahapatra, M. M., *Evolution of phases in P91 steel in various heat treatment conditions and their effect on microstructure stability and mechanical properties*. Materials Science and Engineering A, 2016. **664**: p. 58-74.
35. *I.S. EN 10216-2:2013*. The International Organisation for Standardisation, 2013.
36. Abe, F., Tabuchi, M., Kondo, M., Tsukamoto, S., *Suppression of Type IV fracture and improvement of creep strength of 9Cr steel welded joints by boron addition*. International Journal of Pressure Vessels and Piping, 2007. **84**: p. 44-52.
37. Lee, J.S., Maruyama, K., *Mechanism of Microstructural Deterioration Preceding Type IV Failure in Weldment of Mod.9Cr-1Mo Steel*. Metallurgical Materials International, 2015. **21**: p. 639-645.
38. Shankar, V., Sandhya, R., Mathew, M.D., *Creep-fatigue-oxidation interaction in Grade 91 steel weld joints for high temperature applications*. Materials Science and Engineering A, 2011. **528**: p. 8428-8437.
39. Hamelin, C.J., Muransky, O., Smith, M. C., Holden, T. M., Luzin, V., Bendeich, P. J., Edwards, L., *Validation of a numerical model used to predict phase distribution and residual stress in ferritic steel weldments*. Acta Materialia, 2014. **75**: p. 1-19.
40. Abe, F., Tabuchi, M., Tsukamoto, S., Shirane, T., *Microstructure evolution in HAZ and suppression of Type IV fracture in advanced ferritic power plant steels*. International Journal of Pressure Vessels and Piping, 2010. **87**: p. 598-604.
41. *ISO 9692-1:2013(E)*. The International Organisation for Standardisation, 2013.

42. I.S. EN ISO 2560:2009. The International Organisation for Standardisation, 2009.
43. ISO/TR 17671-2:2002(E). The International Organisation for Standardisation, 2002.
44. ISO/TR 14745:2015(E). The International Organisation for Standardisation, 2015.
45. Yaghi, A.H., Hyde, T. H., Becker, A. A., Williams, J. A., Sun, W., *Residual stress simulation in welded sections of P91 pipes*. Journal of Materials Processing Technology, 2005. **167**: p. 480-487.
46. Li, S., Ren, S., Zhang, Y., Deng, D., Murakawa, H., *Numerical investigation of formation mechanism of welding residual stress in P92 steel multi-pass joints*. Journal of Materials Processing Technology, 2017. **244**: p. 240-252.
47. Varma Prasad, V., Joy Varghese, V., Suresh, M. R., Siva Kumar, D., *3D simulation of residual stress developed during TIG welding of stainless steel pipes*. Procedia Technology, 2016. **24**: p. 364-371.
48. Berglund, D., Alberg, H., Runnelmalm, H., *Simulation of welding and stress relief heat treatment of an aero engine component*. Finite Elements in Analysis and Design, 2003. **39**: p. 865-881.
49. Sattari-Far, I., Javadi, Y., *Influence of welding sequence on welding distortions in pipes*. International Journal of Pressure Vessels and Piping, 2008. **85**: p. 265-274.
50. Smith, M.C., *Advances in weld residual stress prediction: A review of the NeT TG4 simulation round robin part 1, thermal analysis*. International Journal of Pressure Vessels and Piping, 2017.
51. Deng, D., Murakawa, H., *Numerical simulation of temperature field and residual stress in multi-pass welds in stainless steel pipe and comparison with experimental measurements*. Computational Materials Science, 2006. **37**: p. 269-277.
52. Dong, P., *Residual Stress Analyses of a Multi-Pass Girth Weld: 3-D Special Shell Versus Axisymmetric Models*. Journal of Pressure Vessel Technology, 2001. **123**: p. 207-213.
53. Goldack, J., Chakravarti, A., Bibby, M., *A new finite element model for welding heat sources*. Journal of Metallurgical Transactions B, 1984. **15**: p. 299-305.
54. Smith, M.C., Smith, A. C., Wimpory, R., Ohms, C., *A review of the NeT Task Group 1 residual stress measurement and analysis round robin on a single weld bead-on-plate specimen*. International Journal of Pressure Vessels and Piping, 2014. **120-121**: p. 93-140.
55. Brickstad, B., Josefson, B. L., *A parametric study of residual stresses in multi-pass butt-welded stainless steel pipes*. International Journal of Pressure Vessels and Piping, 1998. **75**: p. 11-25.
56. Deshpande, A.A., Tanner, D. W. J., Sun, W., Hyde, T. H., McCartney, G., *Combined butt joint welding and post weld heat treatment simulation using SYSWELD ad ABAQUS*. Proceedings of the Institution of Mechanical Engineers, Part L: Journal of Materials: Design and Applications, 2011. **225**: p. 1-10.
57. Abburi Venkata, K., Truman, C. E., Wimpory, R. C., Pirling, T., *Numerical simulation of a three-pass TIG welding using finite element method with validation from measurements*. International Journal of Pressure Vessels and Piping, 2018. **164**: p. 68-79.
58. Song, S., Pei, X., Dong, P., *An Interpretation of Welding Linear Heat Input for 2D Residual Stress Models*, in ASME Pressure Vessels and Piping Conference PVP20152015: Boston, Massachusetts, USA.
59. Murthy, Y., Venkata Rao, G., Krishna Iyer, P., *Numerical simulation of welding and quenching processes using transient thermal and therm-elasto-plastic formulations*. Computers & Structures, 1996. **60**: p. 131-154.
60. Yaghi, A.H., Hyde, T. H., Becker, A. A., Sun, W., *Finite element simulation of welding and residual stresses in a P91 steel pipe incorporating solid-state phase transformation and post-weld heat treatment*. Journal of Strain Analysis, 2008. **43**: p. 275-293.
61. Yaghi, A.H., Hyde, T. H., Becker, A. A., Sun, W., *Finite element simulation of residual stresses induced by the dissimilar welding of a P92 steel pipe with weld metal IN625*. International Journal of Pressure Vessels and Piping, 2013. **111-112**: p. 173-186.

62. Alberg, H., Berglund, D., *Comparison of plastic, viscoplastic, and creep models when modelling welding and stress relief heat treatment*. Computational Methods in Applied Mechanics and Engineering, 2003. **192**: p. 5189-5208.
63. Chen, S., Guillemot, G., Gandin, C-A., *Three-dimensional cellular automaton-finite element modeling of solidification grain structures for arc-welding processes*. Acta Materialia, 2016. **115**: p. 448-467.
64. Mac Ardghail, P., Harrison, N., Leen, S. B., *A through-process, thermomechanical model for predicting welding-induced microstructure evolution and post-weld high-temperature fatigue response*. International Journal of Fatigue, 2018. **112**: p. 216-232.
65. Sawada, K., Hara, T., Tabuchi, M., Kimura, K., Kubushiro, K., *Microstructure characterisation of heat affected zone after welding in Mod.9Cr-1Mo steel*. Materials Characterisation, 2015. **101**: p. 106-113.
66. Swindeman, R.W., Santella, M. L., Maziasz, P. J., Roberts, B. W., Coleman, K., *Issues in replacing Cr-Mo steels and stainless steels with 9Cr-1Mo-V steel*. International Journal of Pressure Vessels and Piping, 2004. **81**: p. 507-512.
67. Arivazhagan, B., Vasudevan, M., *A comparative study on the effect of GTAW processes on the microstructure and mechanical properties of P91 steel weld joints*. Journal of Manufacturing Processes, 2014. **16**: p. 305-311.
68. Vallourec & Mannesmann Tubes, *V & M Experience in T/P91 Tubes and Pipes*, in *International Workshop on Fabrication & Processing of Grade 91 Material, FAB 912011*: Tiruchirappalli, India.
69. Koistinen, D.P., Marburger, R.E, *A general equation prescribing the extent of the austenite-martensite transformation in pure iron-carbon alloys and plain carbon steels*. Acta Metallurgica, 1959. **7**(1): p. 59-60.
70. Mac Ardghail, P., Barrett, R. A., Harrison, N., Leen, S. B., *Predictions of ICHAZ Cyclic Thermomechanical Response in GTAW Process for 9Cr Steels*. Journal of Pressure Vessel Technology, 2019. **141**: p. 021403.
71. Yu, H.Y., *A New Model for the Volume Fraction of Martensitic Transformations*. Metallurgical and Materials Transactions A, 1997. **28A**: p. 2499-2505.
72. Huyan, F., Hedstrom, P., Hoglund, L., Borgenstam, A.,, *A Thermodynamic-Based Model to Predict the Fraction of Martensite in Steels*. Metallurgical and Materials Transactions A, 2016. **47A**: p. 4404-4410.
73. Steinbach, I., Pezzolla, F., Nestler, B., Seeselberg, M., Prieler, R., Schmitz, G. J., Rezende, J. L. L., *A phase field concept for multiphase systems*. Physica D, 1996. **94**: p. 135-147.
74. Militzer, M., *Phase field modelling of microstructure evolution in steels*. Current Opinion in Solid State and Materials Science, 2011. **15**: p. 106-115.
75. Toloui, M., Militzer M., *Phase field modelling of the simultaneous formations of bainite and ferrite in TRIP steel*. Acta Materialia, 2018. **144**: p. 786-800.
76. Boettger, B., Eiken, J., Apel, M., *Multi-ternary extrapolation scheme for efficient coupling of thermodynamic data to a multi-phase-field model*. Computational Materials Science, 2015. **108**: p. 283-292.
77. Milovic, L., Vuherer, T., Blacic, I., Vrhovac, M., Stankovic, M., *Microstructures and mechanical properties of creep resistant steel for application at elevated temperatures*. Materials and Design, 2013. **46**: p. 660-667.
78. Doherty, R.D., Hughers, D. A., Humphreys, F. J., Jonas, J. J., Juul Jensen, D., Kassner, M. E., King, W. E., McNelley, T. R., McQueen, H. J., Rollett, A. D., *Current issues in recrystallization: a review*. Materials Science and Engineering A, 1997. **238**: p. 219-274.
79. Galindo-Nava, E.I., Rivera-Díaz-del-Catillo, P. E. J., *A model for the microstructure behaviour and strength evolution in lath martensite*. Acta Materialia, 2015. **98**: p. 81-93.

80. Li, H., Lin, J., Dean, T. A., Wen, S. W., Bannister, A. C., *Modelling mechanical property recovery of a linepipe steel in annealing process*. International Journal of Plasticity, 2009. **25**: p. 1049-1065.
81. Lin, J., Dean, T. A., *Modelling of microstructure evolution in hot forming using unified constitutive equations*. Journal of Materials Processing Technology, 2005. **167**: p. 354-362.
82. Lin, J., Liu, Y., *A set of unified microstructure equations for modelling microstructure evolution in hot rolling*. Journal of Materials Processing Technology, 2003. **143-144**: p. 281-285.
83. Estrin, Y., *Dislocation theory based constitutive modelling: foundations and applications*. Journal of Materials Processing Technology, 1998. **80-81**: p. 33-39.
84. Yaowu Shi, D.C., Yongping Lei, Xiaoyan Li, *HAZ microstructure simulation in welding of a ultra fine grain steel*. Computational Materials Science, 2004. **31**: p. 379-388.
85. Wei, H.L., Elmer, J. W., Debroy, T., *Three-dimensional modeling of grain structure evolution during welding of an aluminium alloy*. Acta Materialia, 2017. **126**: p. 413-425.
86. Barrett, R.A., O'Donoghue, P. E., Leen, S. B., *A physically-based constitutive model for high temperature microstructural degradation under cyclic deformation*. International Journal of Fatigue, 2017. **100**: p. 388-406.
87. Armaki, H.G., Chen, R. P., Maruyama, K., Yoshizawa, M., Igarashi, M., *Static recovery of tempered lath martensite microstructures during long term ageing in 9-12% Cr heat resistant steels*. Materials Letters, 2009. **63**: p. 2423-2425.
88. Myhr, O.R., Grong, O., Andersen, S. J., *Modelling of the age hardening behaviour of Al-Mg-Si alloys*. Acta Materialia, 2001. **49**: p. 65-75.
89. Hoang, N.-H., Hopperstad, O. S., Myhr, O. R., Marioara, C., Langseth, M., *An improved nano-scale material model applied in axial-crushing analysis of square hollow section aluminium profiles*. Thin-Walled Structures, 2015. **92**: p. 93-103.
90. Myhr, O.R., Grong, O., Pedersen, K. O., *A combined precipitation, yield strength, and work hardening model for Al-Mg-Si alloys*. Metallurgical and Materials Transactions A, 2010. **41A**: p. 2276-2289.
91. Myhr, O.R., Grong, O., *Modelling of non-isothermal transformations in alloys containing a particle distribution*. Acta Materialia, 2000. **48**: p. 1605-1615.
92. Vadasz, P., Vadasz, A. S., *The neoclassical theory of population dynamics in spatially homogeneous environments (I) Derivation of universal laws and monotonic growth*. Physica A, 2002. **309**: p. 329-359.
93. Barbadikar, D.R., Deshmukh, G. S., Maddi, L., Laha, K., Parameswaran, P., Ballal, A. R., Peshwe, D. R., Paretkar, R. K., Nandagopal, M., Mathew, M. D., *Effect of normalizing and tempering temperatures on microstructure and mechanical properties of P92 steel*. International Journal of Pressure Vessels and Piping, 2015. **132-133**: p. 97-105.
94. Spigarelli, S., *Microstructure-based assessment of creep rupture strength in 9Cr steels*. International Journal of Pressure Vessels and Piping, 2013. **101**: p. 64-71.
95. Galindo-Nava, E.I., Rainforth, W. M., Rivera-Díaz-del-Catillo, P. E. J., *Predicting microstructure and strength of maraging steels: Elemental optimisation*. Acta Materialia, 2016. **117**: p. 270-285.
96. Taneike, M., Kondo, M., Morimoto, T., *Accelerated Coarsening of MX Carbonitrides in 12%Cr steels during Creep Deformation*. ISIJ International, 2001. **41**: p. S111-S115.
97. Rajan, T.V., Sharma, C. P., Sharma, A., *Heat Treatment Principles and Techniques*. 2nd ed 2013, Delhi, India: PHI Learning Private Limited.
98. Armaki, H.G., Chen, R., Kano, S., Maruyama, K., Hasegawa, Y., Igarashi, M., *Strain-induced coarsening of nanoscale precipitates in strength enhanced high Cr ferritic steels*. Materials Science and Engineering A, 2012. **532**: p. 373-380.
99. Mac Ardghail, P., Harrison, N., Leen, S. B., *A process-structure-property model for welding of 9Cr power plant components: The influence of welding process temperatures on in-service*

- cyclic plasticity response*. International Journal of Pressure Vessels and Piping, 2019. **173**: p. 26-44.
100. Huffman, P.J., *A strain energy based damage model for fatigue crack initiation and growth*. International Journal of Fatigue, 2016. **88**: p. 197-204.
  101. Du, Y.-N., Zhu, M.-L., Liu, X., Xuan, F.-Z., *Effect of long-term aging on near-threshold fatigue crack growth of Ni-Cr-Mo-V steel welds*. Journal of Materials Processing Technology, 2015. **226**: p. 228-237.
  102. Zhao, L., Jing, H., Xu, L., Han, Y., Xiu, J., *Effect of residual stress on creep crack growth behaviour in ASME P92 steel*. Engineering Fracture Mechanics, 2013. **110**: p. 233-248.
  103. Rouse, J.P., Sun, W., Hyde, T. H., Morris, A., *Comparative assessment of several creep damage models for use in life prediction*. International Journal of Pressure Vessels and Piping, 2013. **108-109**: p. 81-87.
  104. Smith, M.C., Muránsky, O., Austin, C., Bendeich, P., Xiong, Q., *Optimised modeling of AISI 316L(N) material behaviour in the NeT TG4 international weld simulation and measurement benchmark*. International Journal of Pressure Vessels and Piping, 2018. **164**: p. 93-108.
  105. Shan, X., Davies, C. M., Wangsdan, T., O'Dowd, N. P., Nikbin, K. M., *Thermo-mechanical modelling of a single-bead-on-plate weld using the finite element method*. International Journal of Pressure Vessels and Piping, 2009. **86**: p. 110-121.
  106. Leblond, J.B., Devaux, J., Devaux, J. C., *Mathematical modelling of transformation plasticity in steels I: Case of ideal-plastic phases*. International Journal of Plasticity, 1989. **5(6)**: p. 551-572.
  107. Leblond, J.B., Mottet, G., Devaux, J., Devaux, J. C., *Mathematical models of anisothermal phase transformations in steels, and predicted plastic behaviour*. Materials Science and Technology, 1985. **1**: p. 815-822.
  108. Sun, C.Y., Fang, G., Lei L. P., Zeng, P., *Micromechanics model of martensitic transformation-induced plasticity*. Journal of Materials Processing Technology, 2008. **201**: p. 226-231.
  109. Barrett, R.A., O'Donoghue, P. E., Leen, S. B., *A dislocation-based model for high temperature cyclic viscoplasticity of 9-12Cr steels*. Computational Materials Science, 2014. **92**: p. 286-297.
  110. Alang, N.A., Davies, C. M., Nikbin, K. M., *Low Cycle Fatigue Behaviour of Ex-Service P92 Steel at Elevated Temperature*. Procedia Structural Integrity, 2016. **2**: p. 3177-3184.
  111. Touboul, M., Crepin, J., Rousselier, G., Latourte, F., Leclercq, S., *Identification of Local Viscoplastic Properties in P91 Welds from Full Field Measurements at Room Temperature and 625 °C*. Experimental Mechanics, 2013. **53**: p. 455-468.
  112. Esposito, L., Bonora, N., *A primary creep model for Class M materials*. Materials Science and Engineering A, 2011. **528**: p. 5496-5501.
  113. Kloc, L., Sklenicka, V., *Transition from power-law to viscous creep behaviour of P-91 type heat-resistant steel*. Materials Science and Engineering A, 1997. **234-236**: p. 962-965.
  114. Chen, W., Wang, F., Kitamura, T., Feng, M., *A modified unified viscoplasticity model considering time-dependent kinematic hardening for stress relaxation with effect of loading history*. International Journal of Mechanical Sciences, 2017. **133**: p. 883-892.
  115. Benaarbia, A., Rouse, J. P., Sun, W., *A thermodynamically-based viscoelastic-viscoplastic model for the high temperature cyclic behaviour of 9-12% Cr steels*. International Journal of Plasticity, 2018. **107**: p. 100-121.
  116. Khayatzadeh, S., Tanner, D. W. J., Truman, C. E., Flewitt, P. E. J., *Creep deformation and stress relaxation of a martensitic P92 steel at 650°C*. Engineering Fracture Mechanics, 2017. **175**: p. 57-71.
  117. Farragher, T.P., Scully, S., O'Dowd, N. P., Leen, S. B., *Development of life assessment procedures for power plant headers operated under flexible loading scenarios*. International Journal of Fatigue, 2013. **49**: p. 50-61.
  118. Farragher, T.P., Scully, S., O'Dowd, N. P., Hyde, C. J., Leen, S. B., *High Temperature, low cycle fatigue characterisation of P91 weld and heat affected zone material*. Journal of Pressure Vessel Technology, 2014. **136**: p. 021403-1 - 021403-10.

119. Li, M., Barrett, R. A., Scully, S., Harrison, N. M., Leen, S. B., O'Donoghue, P. E., *Cyclic plasticity of welded P91 material for simple and complex power plant connections*. International Journal of Pressure Vessels and Piping, 2016. **87**: p. 391-404.
120. Hall, F.R., Hayhurst, D. R., *Continuum Damage Mechanics Modelling of High Temperature Deformation and Failure in a Pipe Weldment*. Proceedings: Mathematical and Physical Sciences, 1991. **433**: p. 383-403.
121. Hayhurst, R.J., Mustata, R., Hayhurst, D. R., *Creep constitutive equations for parent, Type IV, R-HAZ, CGHAZ and weld material in the range 565-640°C for Cr-Mo-V weldments*. International Journal of Pressure Vessels and Piping, 2005. **82**: p. 137-144.
122. Hayhurst, D.R., Hayhurst, R. J., Vakili-Tahami, F., *Continuum damage mechanics predictions of creep damage initiation and growth in ferritic steel weldments in a medium bore branched pipe under constant pressure at 590°C using a five-material weld model*. Proceedings of the Royal Society A, 2005. **461**: p. 2303-2326.
123. Perrin, I.J., Hayhurst, D. R., *Continuum damage mechanics analyses of type IV creep failure in ferritic steel crossweld specimens*. International Journal of Pressure Vessels and Piping, 1999. **76**: p. 599-617.
124. Das, C.R., Albert, S. K., Bhaduri, A. K., Srinivasan, G., Murty, B. S., *Effect of prior microstructure on microstructure and mechanical properties on modified 9Cr-1Mo steel weld joints*. Materials Science and Engineering A, 2008. **477**: p. 185-192.
125. Pandey, C., Mahapatra, M. M. , Kumar, P., Saini, N., Srivastava, A., *Microstructure and mechanical property relationship for different heat treatment and hydrogen level in multi-pass welded P91 steel joint*. Journal of Manufacturing Processes, 2017. **28**: p. 220-234.
126. Pandey, C., Saini, N., Mahapatra, M., Kumar, P., *Hydrogen induced cold cracking of creep resistant ferritic P91 steel for different diffusible hydrogen levels in deposited metal*. International Journal of Hydrogen Energy, 2016. **41**: p. 17695-17712.
127. Selvi, S.P., Sakthivel, T., Parameswaran, P., Laha, K., *Effect of Normalization Heat Treatment on Creep and Tensile Properties of Modified 9Cr-1Mo Steel*. Transactions of the Indian Institute of Metals, 2016. **69**: p. 261-269.
128. Huang, B., Zhang, J., Wu, Q., *Microstructure and mechanical properties of China low activation martensitic steel joint by TIG multi-pass welding with a new filler wire*. Journal of Nuclear Materials, 2017. **490**: p. 115-124.
129. Zielinska-Lipiec, A., Czyska-Filemonowicz, A., *Characterisation of the Micro- and Nanoscale Structure of New Creep-Resistant Steels for Use in Advanced USC Steam Power Plants*. Materials Transactions, 2007. **48**: p. 931-935.
130. Sun, F., Meade, E. D., O'Dowd, N. P., *Microscale modelling of the deformation of a martensitic steel using the Voronoi tessellation method*. Journal of the Mechanics and Physics of Solids, 2018. **113**: p. 35-55.
131. Wei, X., Asgari, S. A., Wang, J. T., Rolfe, B. F., Zhu, H. C., Hodgson, P. D., *Micromechanical modelling of bending under tension forming behaviour of dual phase steel 600*. Computational Materials Science, 2015. **108**: p. 72-79.
132. Galindo-Nava, E.I., Rivera-Díaz-del-Catillo, P., *Understanding martensite and twin formation in austenitic steels: A model describing TRIP and TWIP effects*. Acta Materialia, 2017. **128**: p. 120-134.
133. Li, M., Wang, L., Almer, J. D., *Dislocation evolution during tensile deformation in ferritic-martensitic steels revealed by high-energy X-rays*. Acta Materialia, 2014. **76**: p. 381-393.
134. Babu, B., Lindgren, L-E., *Dislocation density based model for plastic deformation and globularisation of Ti-6Al-4V*. International Journal of Plasticity, 2013. **50**: p. 94-108.
135. Ó Murchú, C., Leen, S. B., O'Donoghue, P., Barrett, R. A., *A precipitate evolution-based continuum damage mechanics model of creep behaviour in welded 9Cr steel at high temperature* Proceedings of the Institution of Mechanical Engineers, Part L: Journal of Materials: Design and Applications, 2019. **233**: p. 39-51.

136. Ó Murchú, C., Leen, S. B., O'Donoghue, P., Barrett, R. A., *A physically-based creep damage model for effects of different precipitate types*. Materials Science and Engineering A, 2017. **682**: p. 714-722.
137. Evers, L.P., Parks, D. M., Brekelmans, W. A. M., Geers, M. G. D., *Crystal plasticity model with enhanced hardening by geometrically necessary dislocation accumulation*. Journal of the Mechanics and Physics of Solids, 2002. **50**: p. 2403-2424.
138. Roters, F., Eisenlohr, P., Hantcherli, L., Tjahjanto, D. D., Bieler, T. R., Raabe, D., *Overview of constitutive laws, kinematics, homogenisation and multiscale methods in crystal plasticity finite-element modelling: Theory, experiments, applications*. Acta Materialia, 2010. **58**: p. 1152-1211.
139. Turteltaub, S., Suiker, A. S. J., *Transformation-induced plasticity in ferrous alloys*. Journal of Mechanics and Physics of Solids, 2005. **53**: p. 1747-1788.
140. Li, D.-F., Barrett, Richard A., O'Donoghue, Padraic E., O'Dowd, Noel P., Leen, Sean B., *A multi-scale crystal plasticity model for cyclic plasticity and low-cycle fatigue in a precipitate-strengthened steel at elevated temperature*. Journal of Mechanics and Physics of Solids, 2017. **101**: p. 44-62.
141. Li, M., Barrett, O'Donoghue, P. E., Leen, S. B., *Microstructure modeling of high-temperature microcrack initiation and evolution in a welded 9Cr martensitic steel*. Proceedings of the Institution of Mechanical Engineers, Part L: Journal of Materials: Design and Applications, 2019. **223**: p. 2160-2174.
142. Li, D.-F., Barrett, R. A., O'Donoghue, P. E., Hyde, C. J., O'Dowd, N. P., Leen, S. B., *Micromechanical finite element modelling of thermo-mechanical fatigue for P91 steels*. International Journal of Fatigue, 2016. **87**: p. 192-202.
143. Skouras, A., Flewitt, P. E., Peel, M., Pavier, M. J., *Residual stress measurements in a P92 steel-IN625 superalloy metal weldment in the as-welded and then after post weld heat treated conditions*. International Journal of Pressure Vessels and Piping, 2014. **123-124**: p. 10-18.
144. Liu, C., Shanthraj, P., Diehl, M., Roters, F., Dong, S., Dong, J., Ding, W., Raabe, D., *An integrated crystal plasticity-phase field model for spatially resolved twin nucleation, propagation and growth in hexagonal materials*. International Journal of Plasticity, 2018. **106**: p. 203-227.
145. Li, D.-F., Golden, B. J., O'Dowd, N. P., *Multiscale modelling of mechanical response in a martensitic steel: A micromechanical and length-scale dependent framework for precipitate hardening*. Acta Materialia, 2014. **80**: p. 445-456.
146. Mohammed, B., Park, T., Pourboghrat, F., Hu, J., Esmailpour, R., Abu-Farha, F., *Multiscale crystal plasticity modeling of multiphase advanced high strength steel*. International Journal of Solids and Structures, 2017.
147. Barroqueiro, B., Pinho-da-Cruz, J., Dias-de-Oliveira, J., Andrade-Campos, A., *A reduced multiscale model for heat treatments in multiphase steels*. Mechanics of Materials, 2016. **102**: p. 7-14.
148. Tjahjanto, D., Roters, F., Eisenlohr, P., *Iso-Work-Rate Weighted-Taylor Homogenisation Scheme for Multiphase Steels Assisted by Transformation-induced Plasticity Effect*. Steel Research International, 2007. **78**: p. 777-783.
149. Yaghi, A.H., Hyde, T. H., Becker, A. A., Sun, W., Hilson, G., Simandjuntak, S., Flewitt, P., Pavier, M., Smith, D., *A Comparison Between Measured and Modeled Residual Stresses in a Circumferentially Butt-Welded P91 Steel Pipe*. Journal of Pressure Vessel Technology, 2010. **132**: p. 011206-1 - 0.11206-10.
150. Dong, P., Song, S., Zhang, J., *Analysis of residual stress relief mechanisms in post-weld heat treatment*. International Journal of Pressure Vessels and Piping, 2014. **122**: p. 6-14.
151. O'Hara, E.M., Harrison, N. M., Polomski, B. K., Barrett, R. A., Leen, S. B., *The effect of inclusions on the high-temperature low-cycle fatigue performance of cast MarBN: Experimental characterisation and computational modelling*. Fatigue and Fracture of Engineering Materials and Structures, 2018. **41**: p. 2288-2304.

152. Potirniche, G., Charit, I., Rink, K., Barlow, F., *Prediction and monitoring systems of creep-fracture behaviour of 9Cr-1Mo steels for reactor pressure vessels*. NEUP 2009 Project, 2013. **09-835**.
153. Barrett, R.A., Hyde, C. J., O'Donoghue, P. E., Leen, S. B., *Thermomechanical fatigue in 9-12Cr steels: Life prediction models and the effect of tensile dwell periods*. International Journal of Fatigue, 2019. **126**: p. 335-245.
154. Rouse, J.P., Hyde, C. J., Morris, A., *A neural network approach for determining spatial and geometry dependent Green's functions for thermal stress approximation in power plant header components*. International Journal of Pressure Vessels and Piping, 2018. **168**: p. 269-288.
155. M. Islam, A.B., M. Rais-Rohani, K. Motoyama, *Simulation-based numerical optimization of arc welding process for reduced distortion in welded structures*. Finite Elements in Analysis and Design, 2014. **84**: p. 54-64.
156. Cerjak, H., *The Role of Welding in the Power Generation Industry*. Proceedings of the International Conference Safety and Reliability of Welded Components, 2008: p. 17-27.
157. Kim, B., Boucard, E., Sourmail, T., San Martín, D., Gey, N., Rivera-Díaz-del-Castillo, P. E. J., *The influence of silicon in tempered martensite: Understanding the microstructure-properties relationship in 0.5–0.6 wt.% C steels*. Acta Materialia, 2014. **68**: p. 169-178.
158. Hutchinson, B., Hagstrom, J., Karlsson, O., Lindell, D., Tornberg, M., Lindberg, F., Thuvander, M., *Microstructures and hardness of as-quenched martensites (0.1–0.5%C)*. Acta Materialia, 2011. **59**: p. 5845-5858.
159. Swarr, T., Krauss, G., *The effect of structure on the deformation of as-quenched and tempered martensite in an Fe-0.2 pct C alloy*. Metallurgical Transactions A, 1976. **7**: p. 41-48.
160. Sklenicka, V., Kucharová, K., Svoboda, M., Kloc, L., Bursík, J., Kroupa, A., *Long-term creep behavior of 9-12%Cr power plant steels*. Materials Characterisation, 2003. **51**: p. 35-48.
161. Talonen, J., Hanninen, H., *Formation of shear bands and strain-induced martensite during plastic deformation of metastable austenitic stainless steels*. Acta Materialia, 2007. **55**: p. 6108-6118.
162. Curtze, S., Kuokkala, V-T., Oikari, A., Talonen, J., Hanninen, H., *Thermodynamic modeling of the stacking fault energy of austenitic steels*. Acta Materialia, 2011. **59**: p. 1068-1076.
163. Ullrich, C., Eckner, R., Kruger, L., Martin, S., Klemm, V., Rafaja, D., *Interplay of microstructure defects in austenitic steel with medium stacking fault energy*. Materials Science and Engineering A, 2016. **649**: p. 390-399.
164. Weidner, A., Segel, C., Biermann, H., *Magnitude of shear of deformation-induced  $\alpha'$  - martensite in high-alloy metastable steel*. Materials Letters, 2015. **143**: p. 155-158.
165. Jin, J.-E., Lee, Y-K., *Effects of Al on microstructure and tensile properties of C-bearing high Mn TWIP steel*. Acta Materialia, 2012. **60**: p. 1680-1688.
166. Renard, K., Idrissi, H., Schryvers, D., Jacques, P. J., *On the stress state dependence of the twinning rate and work hardening in twinning-induced plasticity steels*. Scripta Materialia, 2012. **66**: p. 966-971.
167. Gutierrez-Urrutia, I., Raabe, D., *Dislocation and twin substructure evolution during strain hardening of an Fe-22 wt.% Mn–0.6 wt.% C TWIP steel observed by electron channeling contrast imaging*. Acta Materialia, 2011. **59**: p. 6449-6462.
168. Werner, E., *Solid solution and grain size hardening of nitrogen-alloyed austenitic steels*. Materials Science and Engineering A, 1988. **101**: p. 93-98.
169. Grassel, O., Kuger, L., Frommeyer, G., Meyer, L. W., *High strength Fe-Mn-(Al, Si) TRIP/TWIP steels development - properties - application*. International Journal of Plasticity, 2000. **16**: p. 1391-1409.
170. Pierce, D.T., Jiménez, J. A., Bentley, J., Raabe, D., Oskay, C., Wittig, J. E., *The influence of manganese content on the stacking fault and austenite/ $\epsilon$ -martensite interfacial energies in*

- Fe–Mn–(Al–Si) steels investigated by experiment and theory*. Acta Materialia, 2014. **68**: p. 238-253.
171. Vercammen, S., *Processing and tensile behaviour of TWIP steels, microstructural and textural analysis*, 2004, Katholieke Universiteit Leuven, Leuven.
172. Hyde, T.H., Becker, A. A., Sun, W., Williams, J. A., *Finite-element creep damage analyses of P91 pipes*. International Journal of Pressure Vessels and Piping, 2006. **83**: p. 853-863.
173. Orlová, A., Bursik, J., Kuchanová, K., Sklenicka, V., *Microstructural development during high temperature creep of 9% Cr Steel*. Materials Science and Engineering A, 1998. **245**: p. 39-48.
174. Guguloth, K., Swaminathan, J., Roy, N., Ghosh, R. N., *Uniaxial creep and stress relaxation behaviour of modified 9Cr-1Mo steel*. Materials Science and Engineering A, 2017. **684**: p. 683-696.
175. Zhang, Y.-C., Jiang, W., Tu, S-T., Zhang, X-C., Ye, Y-J., *Creep crack growth behaviour analysis of the 9Cr-1Mo steel by a modified creep-damage model*. Materials Science and Engineering A, 2017. **708**: p. 68-76.
176. Shankar, V., Valsan, M., Bhanu Sankara Rao, K., Kannan, R., Mannan, S. L., Pathak, S. D., *Low cycle fatigue behaviour and microstructural evolution of modified 9Cr-1Mo ferritic steel*. Materials Science and Engineering A, 2006. **437**: p. 413-422.
177. Fournier, B., Dalle, F., Sauzay, M., Longour, J., Salvi, M., Caes, C., Tournié, I., Giroux, P-F., Kim, S-H., *Comparison of various 9-12% Cr steels under fatigue and creep-fatigue at high temperature*. Materials Science and Engineering A, 2011. **528**: p. 6934-6945.
178. Zhu, B., Chen, H., Militzer, M., *Phase-field modelling of cyclic phase transformations in low-carbon steels*. Computational Materials Science, 2015. **108**: p. 333-341.
179. Mai, W., Soghrati, S., *New phase field model for simulating galvanic and pitting corrosion processes*. Electrochimica Acta, 2018. **260**: p. 290-304.
180. Shi, L., Alexandratos, S. A., O'Dowd, N. P., *Prediction of prior austenite grain growth in the heat-affected zone of a martensitic steel during welding*. International Journal of Pressure Vessels and Piping, 2018.
181. Fromm, B.S., Chang, K., McDowell, D. L., Chen, L-Q., Garmestani, H., *Linking phase-field and finite-element modeling for process-structure-property relations of a Ni-based superalloy*. Acta Materialia, 2012. **60**: p. 5984-5999.

### Table caption list

Table 1	Some examples of reported P91 composition (wt. %).
Table 2	Some examples of reported P92 composition (wt. %).
Table 3	Some examples of reported P91 heat treatments.
Table 4	Some examples of FE element numbers from samples in the literature.
Table 5	Examples of PFM modelling domains from literature sources.

### Figure caption list

Fig. 1	A comparison between power plant operating conditions (in black and white – Sub-critical is on the left and ultra-super-critical ‘B’ is on the right) and the net plant efficiency, reproduced from Potirniche et al. [152].
Fig. 2	A representation of the different metallurgical zones present in a welded joint with the corresponding phase diagram for 9Cr steels. Figure reproduced from Cerjak et al. [156].
Fig. 3	A comparison between annealing time at 700°C and grain size (model: solid line, test data: points). Figure reproduced from Li et al. [80].
Fig. 4	3D predictions of fusion-zone and HAZ grain evolution during welding of aluminium 1050A at different weld-torch speeds using the Monte-Carlo method. Note the different grain morphologies. Figure reprinted from Wei et al. [85], with permission from Elsevier.
Fig. 5	A comparison between the lath-width and carbon content of 2.3% Si martensitic steel (Kim et al. [157]), 0.2-1.3%Cr steel (Hutchinson et al. [158]), 0.2%C steel (Swarr & Krauss [159]) and 9-12%Cr steel (Ghassemi-Armaki et al. [87]) and a lath-width and carbon content microstructure model. Figure reprinted from Galindo-Nava et al. [79], with permission from Elsevier.
Fig. 6	A comparison between measured and predicted values for precipitate radius ( $r$ ) and number density ( $N$ ). Figure reprinted from Myhr et al. [88], with permission from Elsevier.
Fig. 7	An illustration of the advantage of a hyperbolic sine (sinh) law over power-law functions. A single sinh law fits the test data (points, [160]) whereas two power-law functions are required. This figure (data and sinh fit) is reproduced from Barrett et al. [109] and supplemented with power-law fits.
Fig. 8	Modelling of the HAZ as (a) a single material region or (b) as three material regions (ICHAZ, FGHAZ and CGHAZ). Reprinted from (a) Li et al. [119], with permission from Elsevier, and (b) Touboul et al. [111], with permission from Society for Experimental Mechanics.
Fig. 9	A comparison of modelled and tested yield stresses for a variety of steels: (a) 301LN steel and (b) 304SS [161], (c) 204SS [162], (d) Fe16Cr6Mn9Ni [163, 164], (e) Fe-(12-30)Mn-(0-1.4)Al-(0-1.2)C [165-167], (f) FeCrNiMn-(0.24-0.56)N [168] and (g) Fe-20Mn-3Al-3Si [169-171], using a single physically-based model, from Galindo et al. [132]. The solid line represents a perfect match and the dotted lines represent deviations of 15%.
Fig. 10	Comparison of model and experimental results for strain and dislocation-density. Figures reprinted from (a) Li et al. [133] (note that N&T: Normalised and tempered, CW: Cold-worked) and (b) Hosseini and Kazeminezhad [24] (note that CGP stands for Constrained Groove Pressing) with permission from Elsevier.
Fig. 11	Comparison of a physically-based creep model against test data (a)600°C [172] and (b)625°C [173]. Figures reprinted from Ó Murchú et al. [136], with permission from Elsevier.

Fig. 12	Comparison of measured (DHD) and predicted residual (a) axial and (b) hoop stresses along the WCL of a welded 316H stainless steel , from the inner pipe wall to the outer wall. Figure after Song et al. [58].
Fig. 13	Comparison of measured (DHD) and predicted residual (a) axial and (b) hoop stresses along the WCL of welded P91, from the inner pipe wall to the outer wall. Figure after Yaghi et al. [149].
Fig. 14	Comparison of measured (DHD) and predicted residual hoop stresses along the WCL of welded P91 (a) before and (b) after PWHT, from the outside pipe wall to the inner wall. Figure after Dong et al. [150].

Table 1. Some examples of reported P91 composition (wt. %).

Element	Reference source						
	Potirniche et al. [152]	Hurtado-Norena et al. [32]	Fournier et al. [29]	Guguloth et al. [174]	Zhang et al. [175]	Shankar et al. [176]	Shankar et al. [38]
Cr	8.55	8.21	8.776	9.4	8.36	8.2	9.3
Mo	0.88	0.9	0.915	1	0.93	0.92	0.99
V	0.21	0.213	0.191	0.25		0.13	0.25
Nb	0.08	0.085	0.078	0.09		0.09	0.1
C	0.1	0.11	0.088	0.08	0.1	0.11	0.11
Mn	0.51	0.36	0.354	0.39		0.48	
Cu	0.18	0.15				0.05	
Si	0.32	0.26	0.329	0.5	0.49	0.3	
N	0.035	0.061	0.043	0.03		0.051	0.068
Ni	0.15	0.15		0.13		0.12	0.14
P	0.012			0.02	0.008	0.018	0.02
S	0.005			0.01	0.002	0.005	0.008
Ti	0.002						
Al	0.007	0.011		0.23			
Zr	0.001						
Sn		0.009					
Co						0.015	
Fe				Balance			

Table 2. Some examples of reported P92 composition (wt. %).

Element	Reference source				
	Yaghi et al., Khayat-zadeh et al. [61, 116]	Barbadikar et al. [93]	Fournier et al. [177]	Xue et al. [31]	Abe et al. [40]
Cr	8.62	9.38	8.68	8.84	8.72
Mo	0.33	0.506	0.37	0.5	0.45
V	0.21	0.215	0.19	0.21	0.21
Nb	0.076	0.075	0.06	0.067	0.06
C	0.1	0.114	0.12	0.12	0.09
Mn	0.45	0.388	0.54	0.43	0.47
Cu		0.0162			
Si	0.45	0.0239	0.23	0.21	0.16
N	0.047	0.0417	0.046	0.042	0.05
Ni	0.27			0.16	
P	0.015	0.012			
S	0.002	0.0035			
Ti					
Al	0.019	0.0076			
W	1.86	1.94	1.59	1.67	1.87
B	0.003	0.0018		0.0033	0.002
Fe			Balance		

Table 3. Some examples of reported P91 heat treatments.

	Reference source					
	Divya et al. [33]	Barbadikar et al. [93]	Lee and Maruyama [37]	Ennis and Czyska-Filemonowisc [23]	Hurtado-Norena et al. [32]	Shankar et al. [38]
Steel grade	P91	P92	P91	P91	P91	P91
Normalising (°C)	1050	1040, 1080	1050	1070	1060	1040
Normalising (minutes)	30	30	60	120	30	60
Tempering (°C)	760	740, 760, 780	780	775	780	760
Tempering (minutes)	60	60	60	120	60	60

Table 4. Some examples of FE element numbers from samples in the literature.

Reference source	Number of elements		Material form	Width/ $D_i$	Thickness	Length
	3D	Axisymmetric				
Li et al. [46]	75,900		Plate	200	6	200
Abhuri Venkata et al. [57]	134,000		Plate	75	18	97
Deng and Murakawa [51]	9,600	300	Pipe	51.15	6	800
Yaghi et al. [60]		13,736	Pipe	45	50	350
Yaghi et al. [61]		2,919	Pipe	147.5	30	700

Note:  $D_i$  = inner diameter

Table 5. Examples of PFM modelling domains from literature sources.

Reference	Model type	Domain size
Toloui and Militzer [75]	2D	36.6 $\mu\text{m}$ $\times$ 36.6 $\mu\text{m}$
	2D	52.2 $\mu\text{m}$ $\times$ 52.2 $\mu\text{m}$
	2D	79.6 $\mu\text{m}$ $\times$ 79.6 $\mu\text{m}$
Boettger et al. [76]	1D	50 $\mu\text{m}$
	2D	1000 $\mu\text{m}$ $\times$ 520 $\mu\text{m}$
Zhu et al. [178]	2D	400 $\mu\text{m}$ $\times$ 400 $\mu\text{m}$
Mai and Soghrati [179]	2D	c. 200 $\mu\text{m}$ $\times$ 300 $\mu\text{m}$
	2D	540 $\mu\text{m}$ $\times$ 500 $\mu\text{m}$
	2D	c. 300 $\mu\text{m}$ $\times$ 250 $\mu\text{m}$
Shi et al. [180]	2D	250 $\mu\text{m}$ $\times$ 250 $\mu\text{m}$
		96 $\mu\text{m}$ $\times$ 36 $\mu\text{m}$ $\times$ 47 $\mu\text{m}$ (PFM only)
Fromm et al. [181]	3D	5 $\mu\text{m}$ $\times$ 5 $\mu\text{m}$ $\times$ 5 $\mu\text{m}$ (PFM and FE)
		10 $\mu\text{m}$ $\times$ 10 $\mu\text{m}$ $\times$ 10 $\mu\text{m}$ (PFM and FE)
		15 $\mu\text{m}$ $\times$ 15 $\mu\text{m}$ $\times$ 15 $\mu\text{m}$ (PFM and FE)

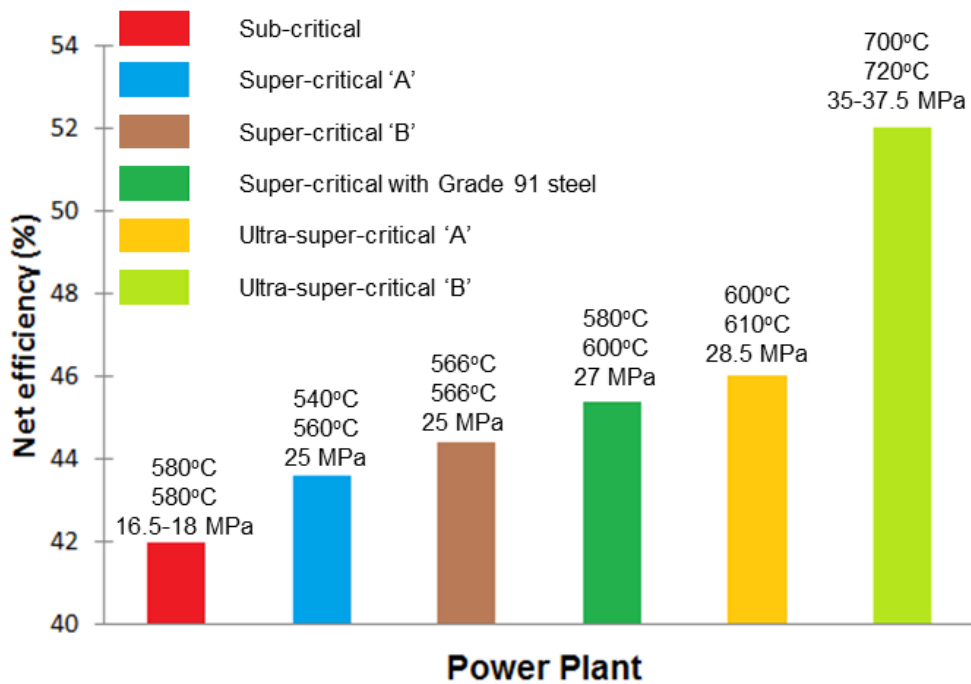


Fig. 1. A comparison between power plant operating conditions (in black and white – Sub-critical is on the left and ultra-super-critical 'B' is on the right) and the net plant efficiency, after Potirniche et al. [152].

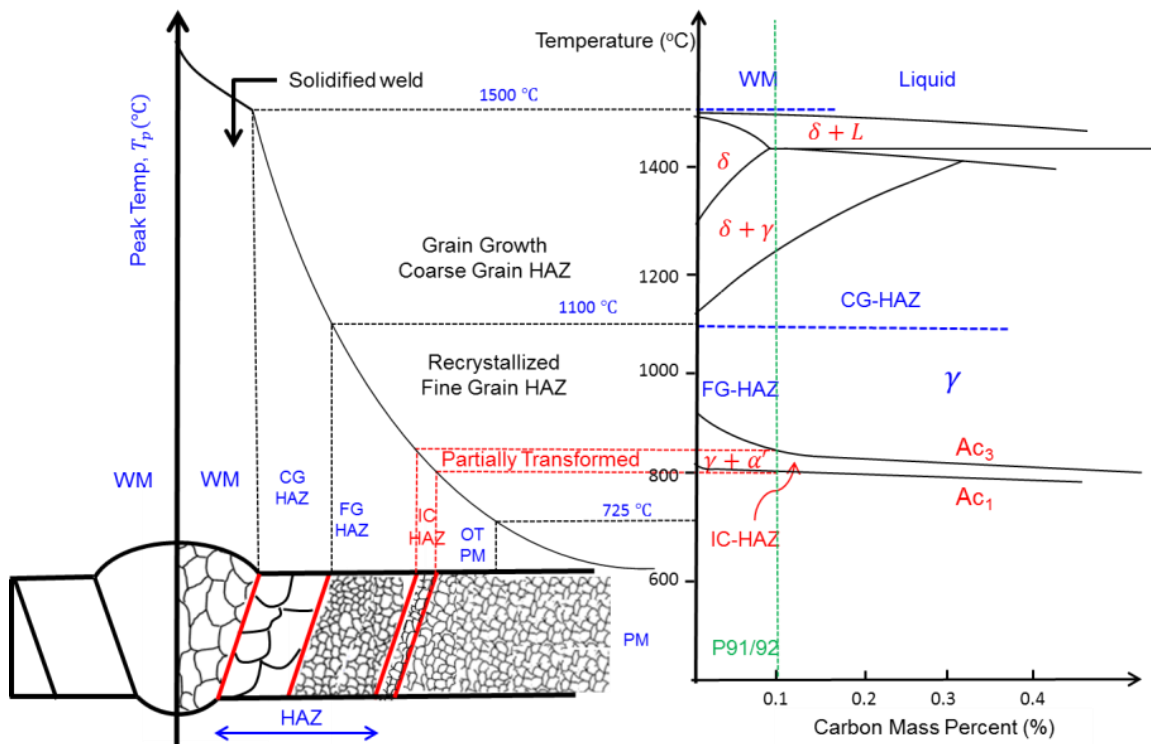


Fig. 2. A representation of the different metallurgical zones present in a welded joint with the corresponding phase diagram for 9Cr steels. Figure reproduced from Cerjak et al. [156].

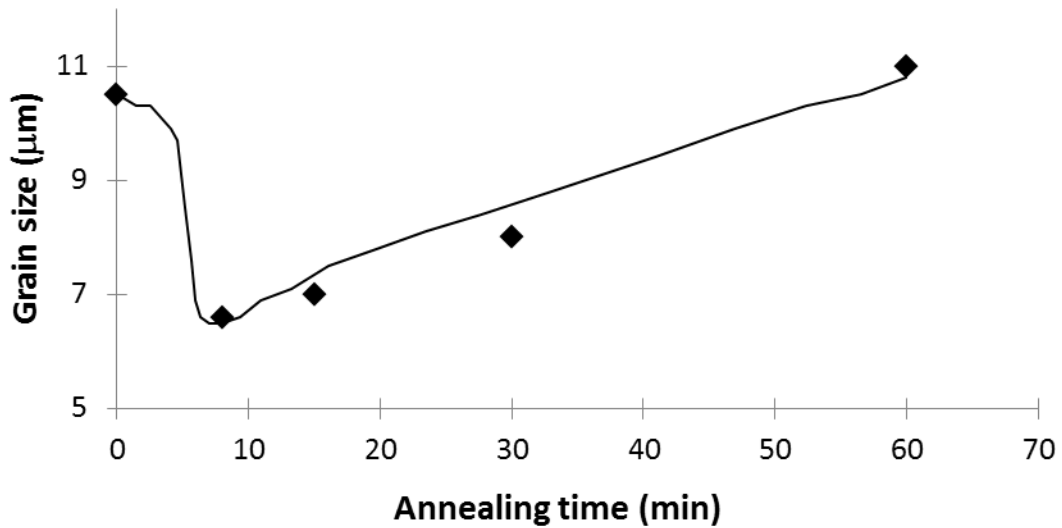


Fig. 3. A comparison between annealing time at 700°C and grain size (model: solid line, test data: points). Figure reproduced from Li et al. [80].

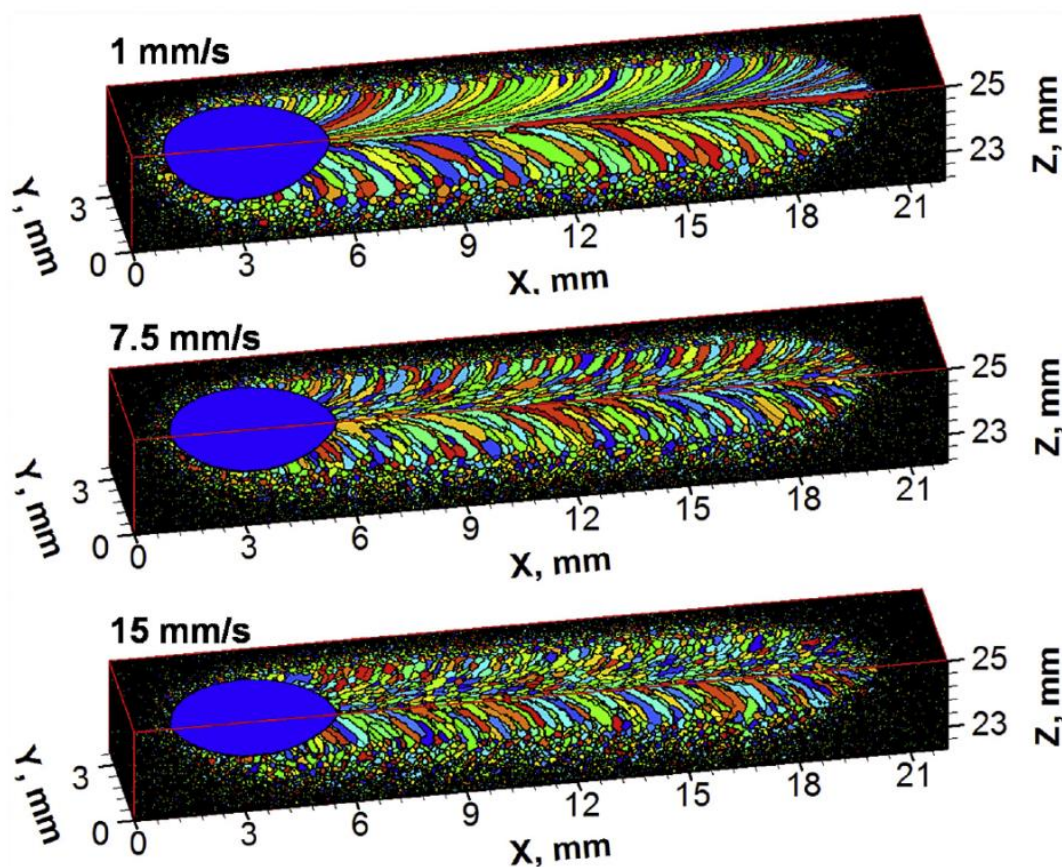


Fig. 4. 3D predictions of fusion-zone and HAZ grain evolution during welding of aluminium 1050A at different weld-torch speeds using the Monte-Carlo method. Note the different grain morphologies. Figure reprinted from Wei et al. [85], with permission from Elsevier.

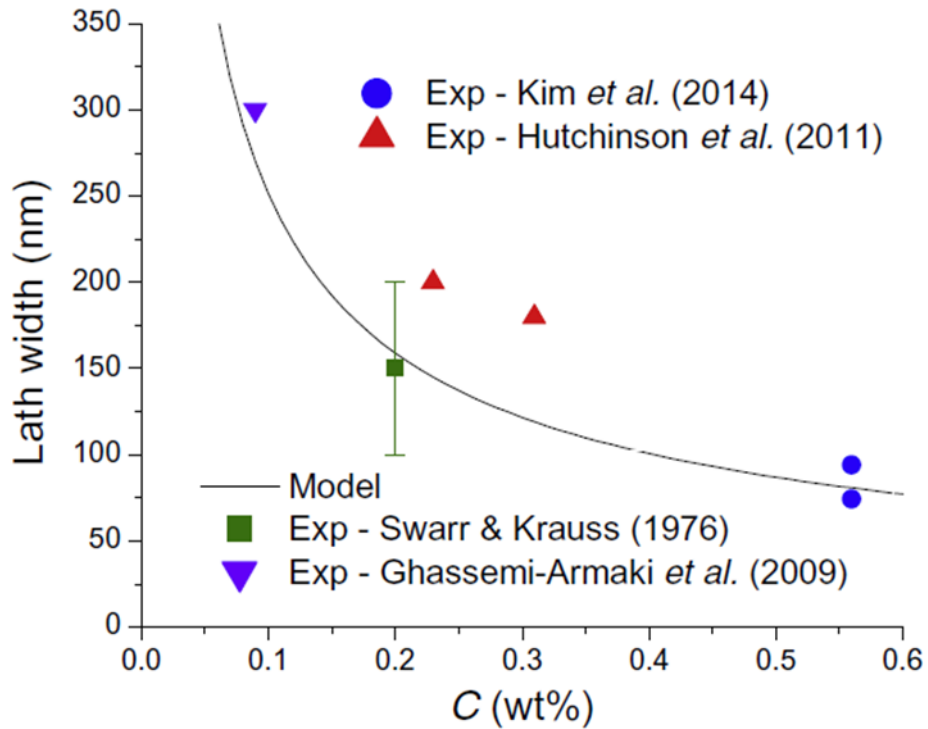


Fig. 5. A comparison between the lath-width and carbon content of 2.3% Si martensitic steel (Kim et al. [157]), 0.2-1.3%Cr steel (Hutchinson et al. [158]), 0.2%C steel (Swarr & Krauss [159]) and 9-12%Cr steel (Ghassemi-Armaki et al. [87]) and a lath-width and carbon content microstructure model. Figure reprinted from Galindo-Nava et al. [79], with permission from Elsevier.

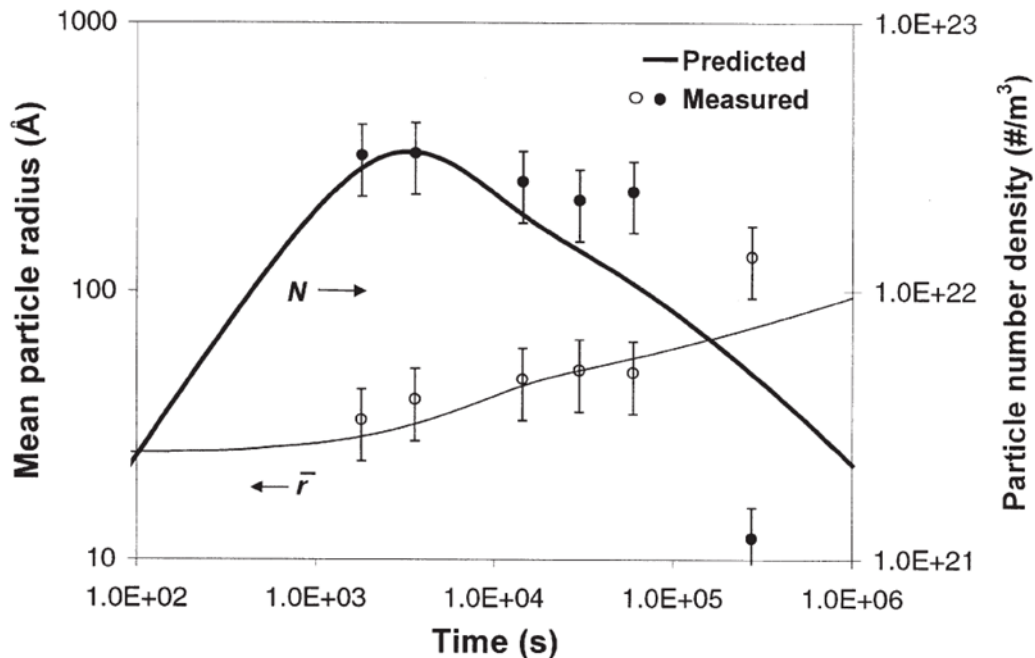


Fig. 6. A comparison between measured and predicted values for precipitate radius ( $\bar{r}$ ) and number density ( $N$ ). Figure reprinted from Myhr et al. [88], with permission from Elsevier.

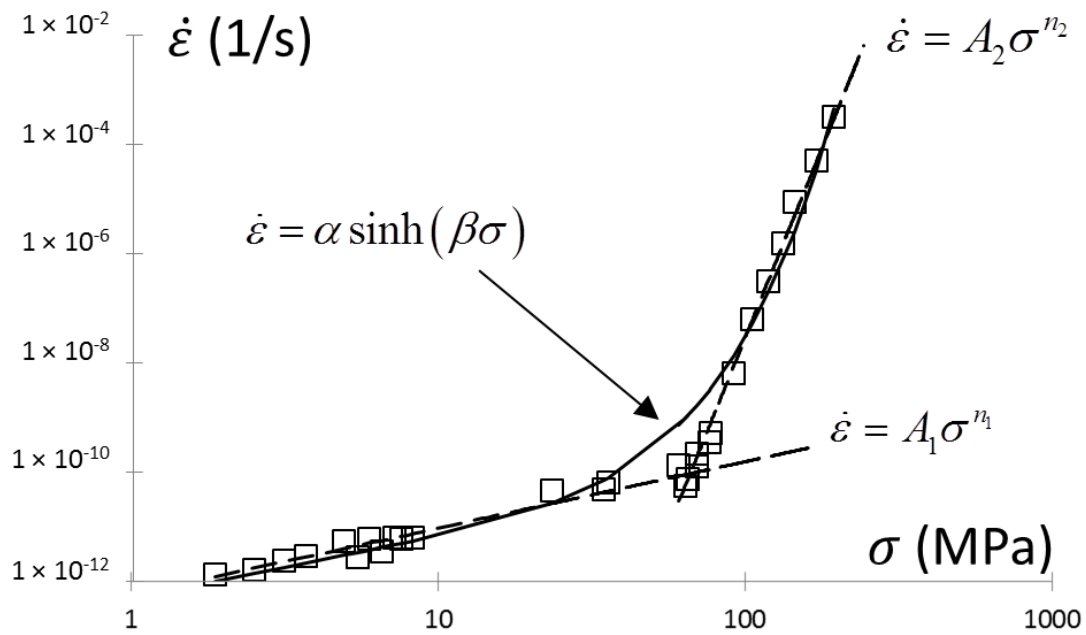


Fig. 7. An illustration of the advantage of a hyperbolic sine (sinh) law over power-law functions. A single sinh law fits the test data (points, [160]) whereas two power-law functions are required. This figure (data and sinh fit) is reproduced from Barrett et al. [109] and supplemented with power-law fits.

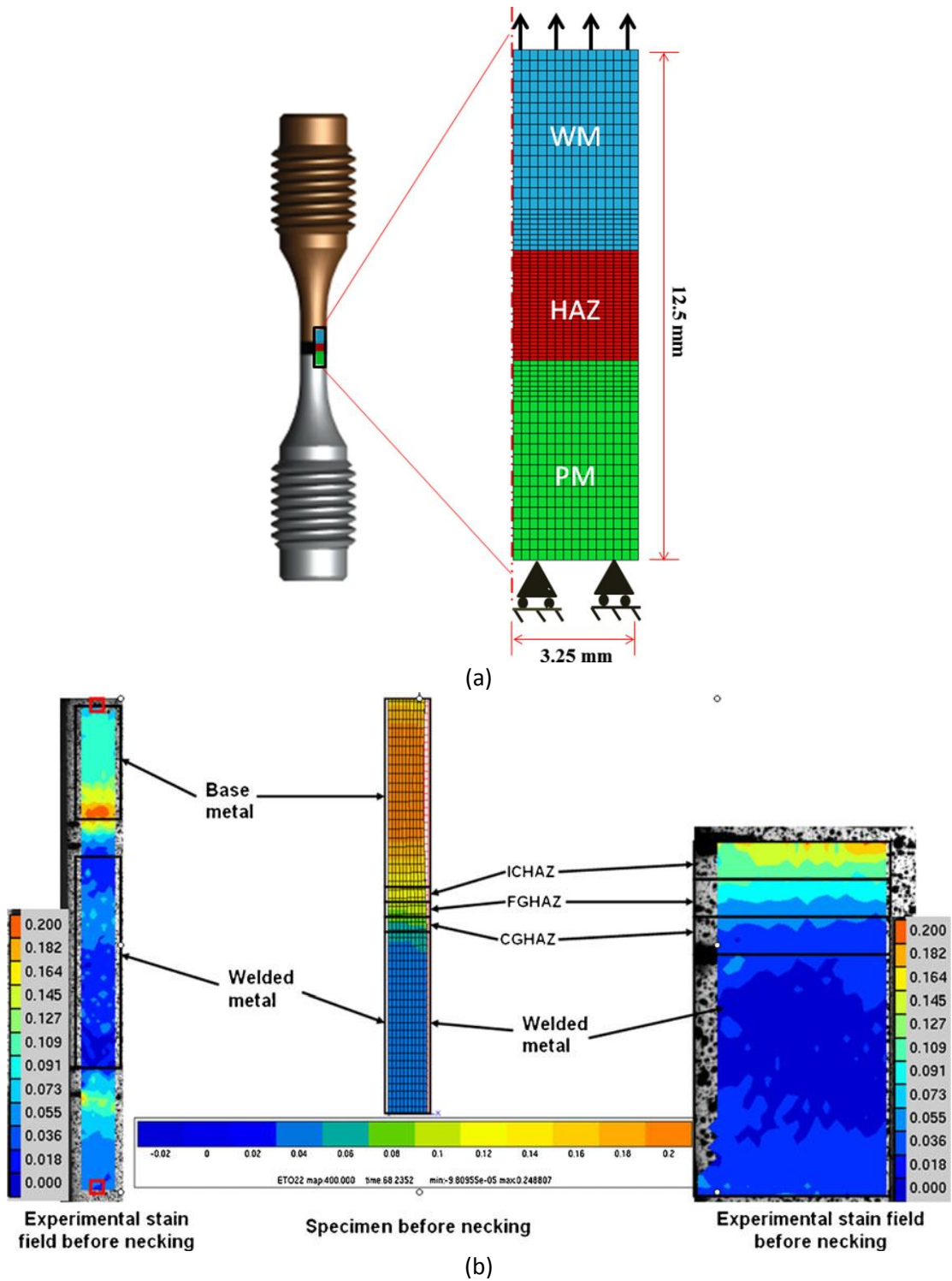


Fig. 8. Modelling of the HAZ as (a) a single material region or (b) as three material regions (ICHAZ, FGHAZ and CGHAZ). Reprinted from (a) Li et al. [119], with permission from Elsevier, and (b) Touboul et al. [111], with permission from Society for Experimental Mechanics.

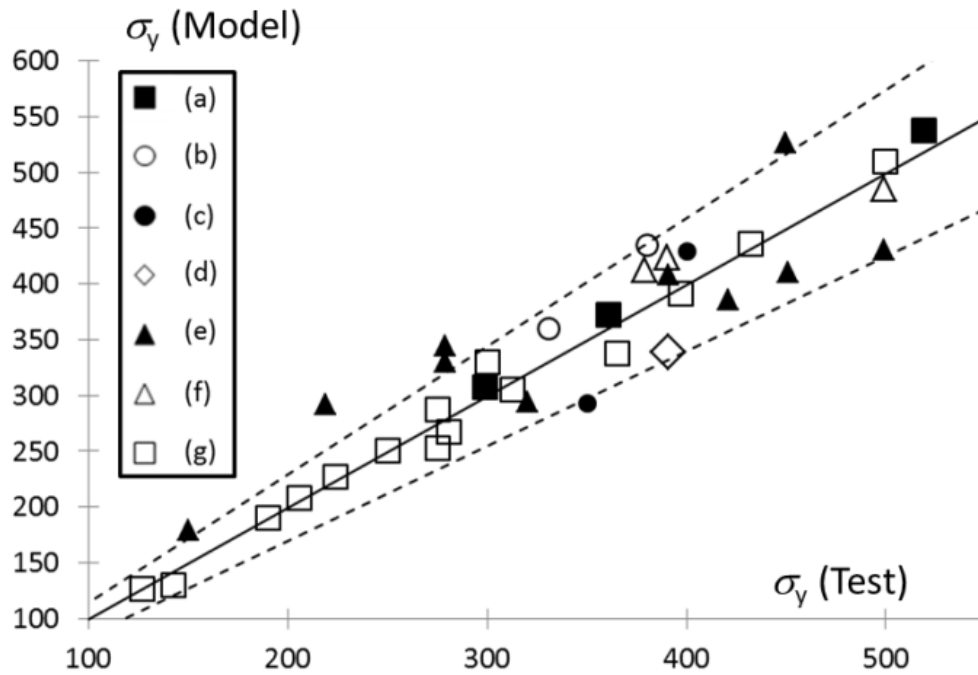


Fig. 9. A comparison of modelled and tested yield stresses for a variety of steels: (a) 301LN steel and (b) 304SS [161], (c) 204SS [162], (d) Fe16Cr6Mn9Ni [163, 164], (e) Fe-(12-30)Mn-(0-1.4)Al-(0-1.2)C [165-167], (f) FeCrNiMn-(0.24-0.56)N [168] and (g) Fe-20Mn-3Al-3Si [169-171], using a single physically-based model, after Galindo et al. [132]. The solid line represents a perfect match and the dotted lines represent deviations of 15%.

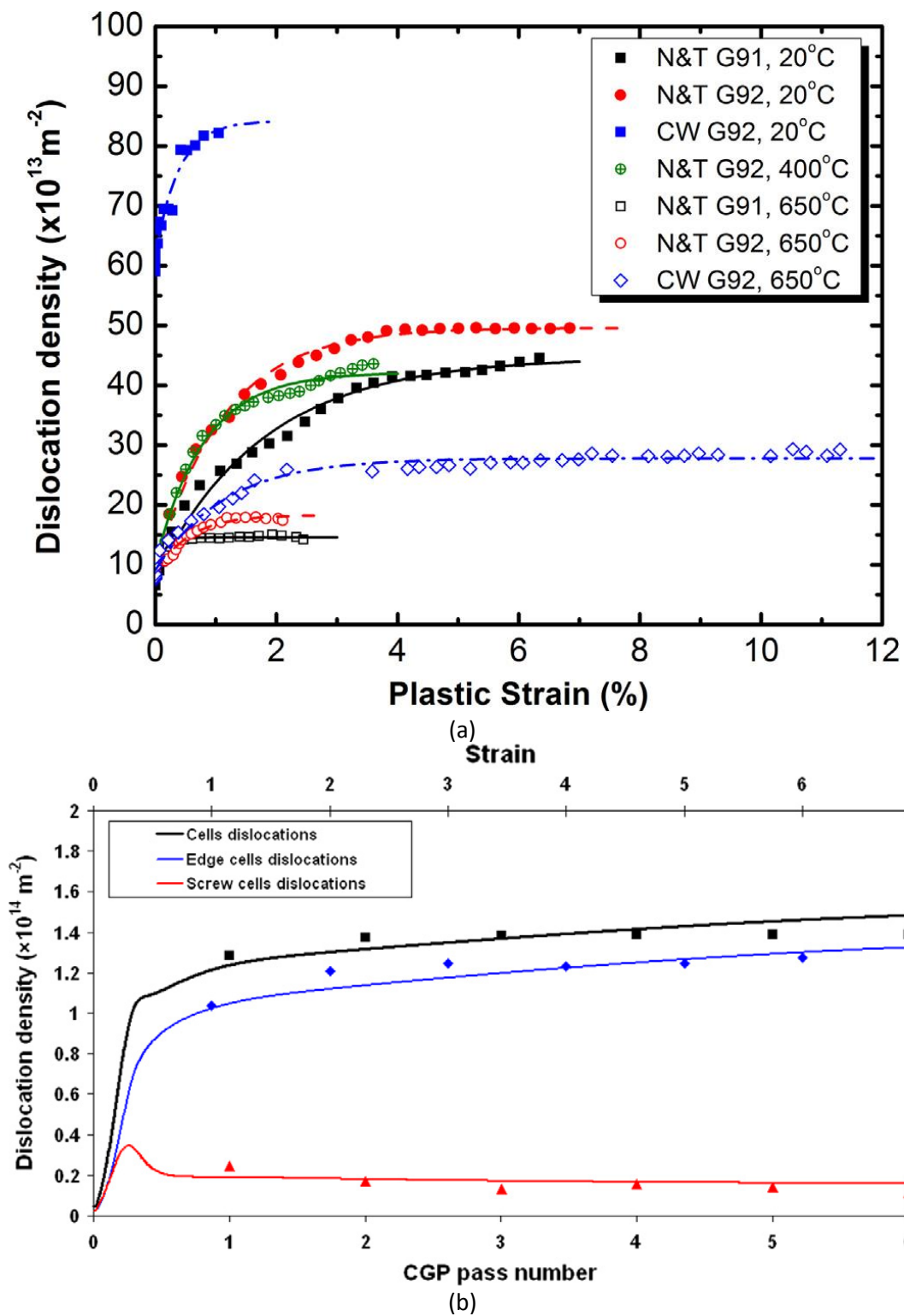
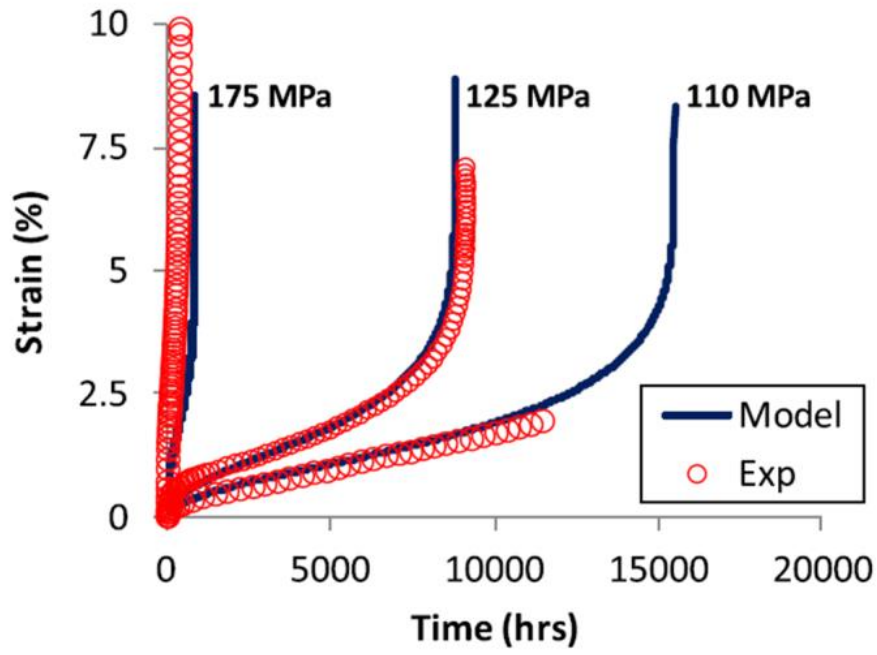
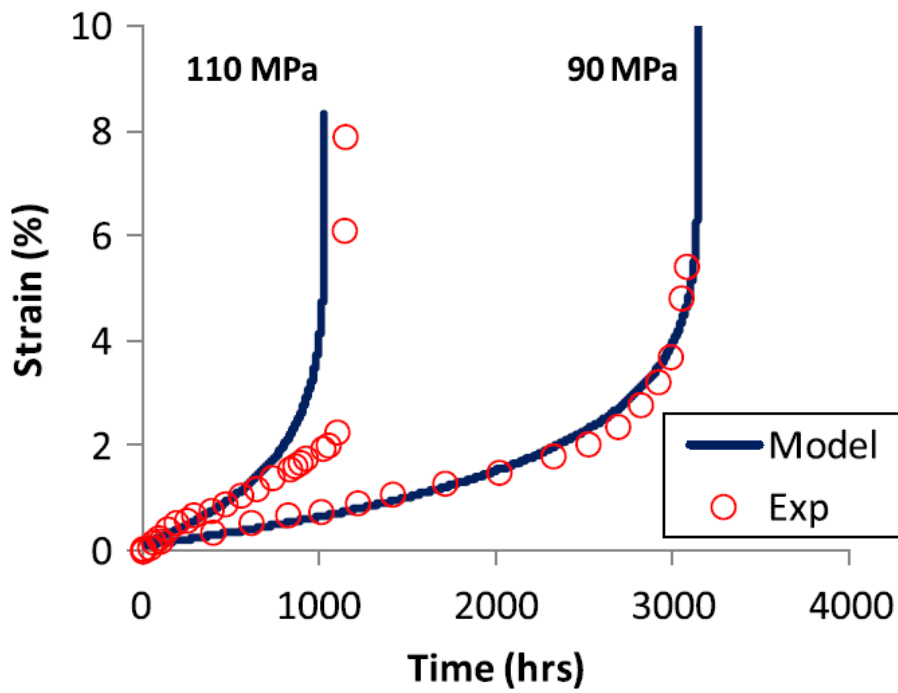


Fig. 10. Comparison of model and experimental results for strain and dislocation-density. Figures reprinted from (a) Li et al. [133] (note that N&T: Normalised and tempered, CW: Cold-worked) and (b) Hosseini and Kazeminezhad [24] (note that CGP: Constrained Groove Pressing) with permission from Elsevier.

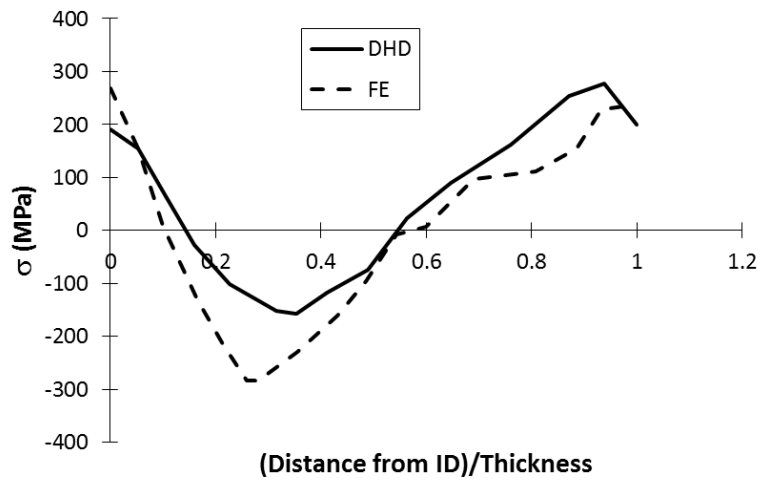


(a)

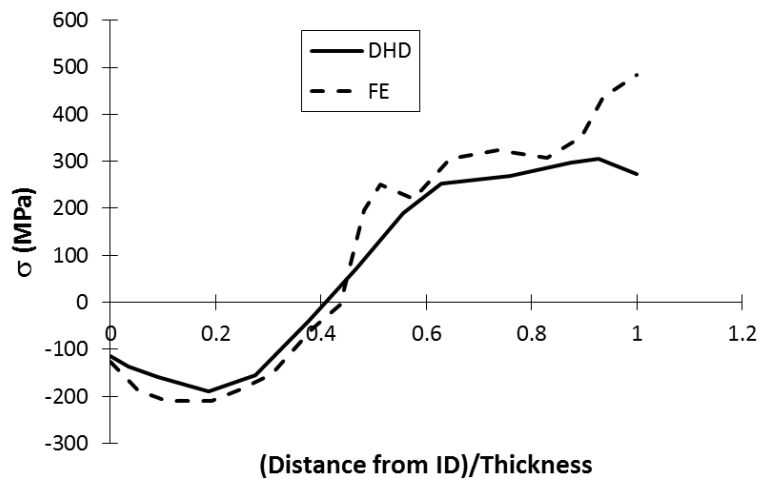


(b)

Fig. 11. Comparison of a physically-based creep model against test data (a)600°C [172] and (b)625°C [173]. Figures reprinted from Ó Murchú et al. [136], with permission from Elsevier.

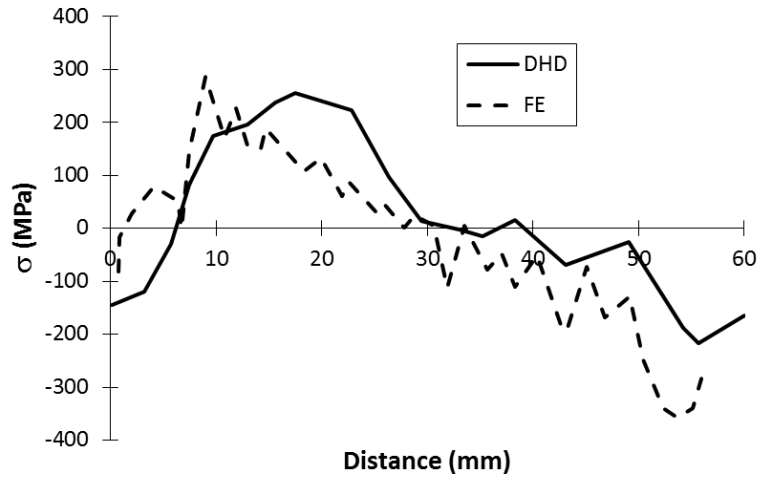


(a)

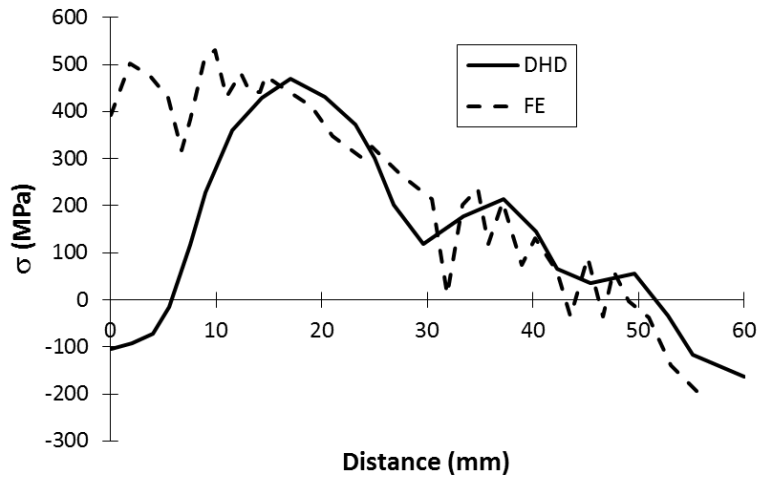


(b)

Fig. 12. Comparison of measured (DHD) and predicted residual (a) axial and (b) hoop stresses along the WCL of a welded 316H stainless steel, from the inner pipe wall to the outer wall. Figure after Song et al. [58].

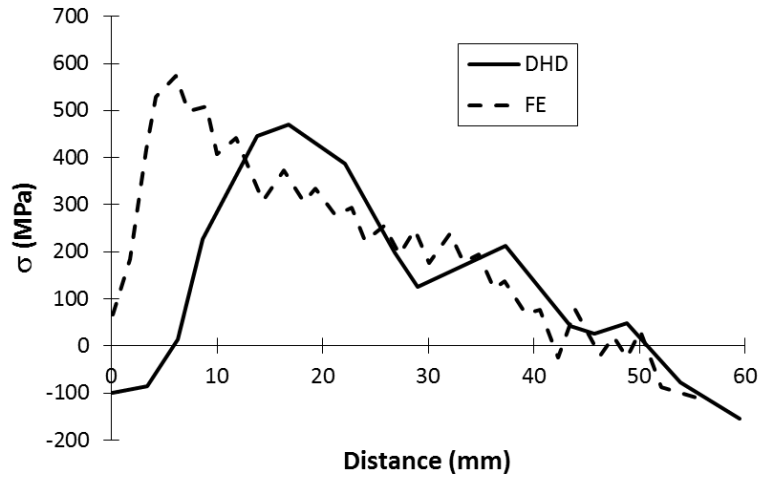


(a)

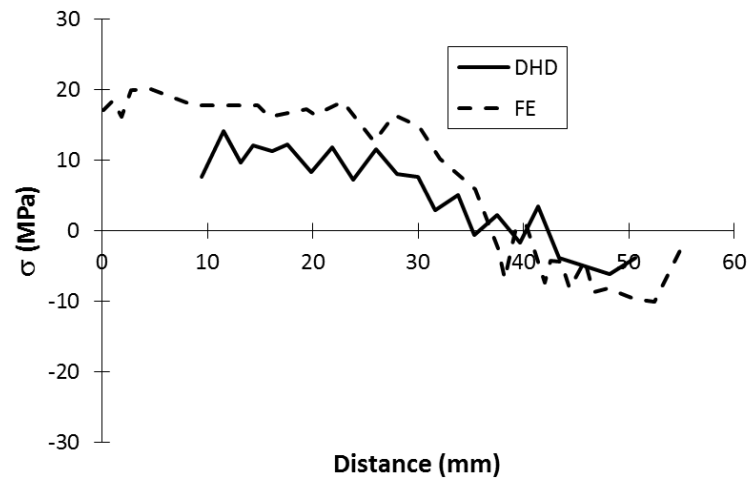


(b)

Fig. 13. Comparison of measured (DHD) and predicted residual (a) axial and (b) hoop stresses along the WCL of welded P91, from the outer pipe wall to the inner wall. Figure after Yaghi et al. [149].



(a)



(b)

Fig. 14. Comparison of measured (DHD) and predicted residual hoop stresses along the WCL of welded P91 (a) before and (b) after PWHT, from the outside pipe wall to the inner wall. Figure after Dong et al. [150].